A nodal-integration based particle finite element method (N-PFEM) to model cliff recession

Jingjing Meng[1], Xue Zhang[2*], Stefano Utili[3], Eugenio Oñate[4]

1. Department of Civil, Environmental and Natural Resources Engineering, Luleå University of Technology, Luleå, Sweden
2. Department of Civil Engineering and Industrial Design, University of Liverpool, Liverpool, United Kingdom
3. School of Engineering, Newcastle University, Newcastle, United Kingdom
4. International Centre for Numerical Methods in Engineering (CIMNE), Barcelona, Spain

Abstract

Cliff recession poses a significant threat to the built environment, transportation infrastructure and land use. In this paper, a novel computational framework called the Nodal-integration based Particle Finite Element Method (N-PFEM) is developed for modelling the cliff recession resulting from weathering-induced landslides. The N-PFEM combines the nodal-integration technique with the PFEM in second-order cone programming and thus requires no variable mapping operation, which is essential in the classical PFEM for modelling history-dependent materials, for modelling large deformation problems such as landslides in cliff recession processes. To verify the developed N-PFEM, a series of benchmarks have been simulated including the cliff recession under both the weathering-limited and transport-limited conditions. Simulation results from the N-PFEM are validated in detail to these from the limit analysis method, well established geomorphologic models and the discrete element method. Additionally, measures for preventing cliff recession such as the construction of retaining wall structures are also investigated using the N-PFEM.

Keywords: Cliff recession, Landslide, PFEM, Nodal integration

----

* Email address: xue.zhang2@liverpool.ac.uk

1. Introduction

Modelling the progressive retreat of cliffs has recently received considerable attention by the engineering community due to increasing coastal erosive processes caused by climate change and amplified environmental awareness at national and European level (Bray and Hooke, 1997). Also the insurance industry needs reliable models for the predictions of the amount of cliff retreat over time for residential buildings located in exposed areas whereas local authorities and decision makers need to know the level of risk faced by residential buildings and public infrastructure (e.g. coastal roads, pedestrian footpaths, car parks, etc.). Along many coastal areas, the recession rate of cliffs is significantly high leading to non-negligible socio-economic impacts (Bird, 2016). A typical example is the soft glacial drift cliff at Holderness coast, Aldbrough, UK, that erodes at about 2 meter per year with a maximum recession rate being 3.4 meter per year (Hobbs et al., 2020). This rapid erosion results in critical impacts on human communities including, but are not limited to, the loss of farmland, damage to infrastructure, properties and tourism. In order to engineer adequate mitigation and remediation measures, it is thus of vital importance to develop reliable models to predict cliff recession rates driven by the local environmental conditions.

The natural drivers responsible for triggering cliff recession can be classified into two categories: factors increasing the driving forces, such as seismic loading (Massey et al., 2017), wave loading (Sunamura, 1982) and anthropogenic activities (Xue et al., 2009), and factors decreasing resistance forces, such as weathering (Utili and Crosta, 2011a) and crack formation (Kogure et al., 2006, Voulgari and Utili, 2017). This paper focuses on the latter and on weathering-induced cliff recession in particular. Indeed, weathering proceeds in the manner of physical break down and chemical alteration of rocks which weakens the shear strength of rocks and form thick sequences of weathered geo-materials whose engineering properties have been highly altered. The weathering process gradually decreases the stability of the slope, which ultimately leads to subsequent landslides and the progressive retreat of the cliff crest (Hutchinson, 2001). The earliest effort devoted to forecasting the progressive evolution of cliff erosion lies in (Fisher, 1866) in which a model was proposed to study the disintegration of a coastal chalk cliff considering the accumulation of a basal debris apron. This model was then extended by further introducing the effect of different weathering stages (Lehmann, 1933) and the upper and lower sloping sectors (Bakker and Le Heux, 1946, Nash, 1981). In these models, the evolution process is controlled based on assumptions concerning the geometry of falling blocks, the bulking of geo-materials, the accumulation of debris and the weathering rate. Further consideration of the effects of mechanical properties of geo-materials on the evolution process were performed in Andrews and Bucknam (1987). More recently, an analytical method based on an upper bound limit analysis approach was proposed to simulate the cliff recession process (Utili and Crosta, 2011a). The basic idea is to perform limit analysis of slope instability induced by a homogeneous decrease of ground strength with the debris following the landslide occurrence being removed before the onset of the successive landslide. This implies weathering-limited slope conditions. Voulgari and Utili (2017) extended the limit analysis model of (Utili and Crosta, 2011a) to account for the effects of seismic actions, the formation of tension cracks and seepage. From their modelling it emerges that although the formation of tension cracks affects the geometry of each landslide profile, it bears little influence on the overall geomorphologic evolution of the cliff especially relative to rock strength degradation. Therefore, the onset of tension crack was not considered in the paper.

Using numerical techniques, cliff recession under more complex conditions, e.g. non uniform slope weathering, have been investigated, such as the evolution of natural cliffs subject to weathering using the discrete element method (Utili and Crosta, 2011a), the evolution of an overhanging rock slope using the displacement discontinuity method (Zhang et al., 2016). These studies, except for Utili and Crosta (2011a, 2011b), focus on the factors triggering slope instabilities leading to cliff recession without attempting to predict the complete evolution of cliff recession that results from a discrete sequence of landslides.

In order to predict the complete evolution process of cliff recession and the resulting geomorphology, the numerical approach adopted has to be capable of predicting not only the failure of a slope but also the post-failure process such as the mass transport and deposition which affects the subsequent slope failures. Recently, several methods have been developed and applied to analyse landslide and granular flow problems such as the smoothed particle hydrodynamics (SPH) method (Bui et al., 2011, Pastor et al., 2014), the material point method (MPM) (Andersen and Andersen, 2010, Soga et al., 2016, Tran and Sołowski, 2019), the finite volume method (FVM) (Mangeney et al., 2003, 2007a) , the discrete element method (DEM) (Staron and Hinch, 2005, Staron, 2008), the dedicated numerical model, SHALTOP, that can consider complex 3D topography (Lucas and Mangeney, 2007, Mangeney et al., 2007b, Favreau et al., 2010), the particle finite element method (PFEM) (Zhang et al., 2014, Wang et al., 2019, Zhang et al., 2019b, Mulligan et al., 2020, Yuan et al., 2020), etc. The PFEM is developed based on the idea that mesh nodes are treated as particles that can move freely and even separate from the domain they originally belong to (Idelsohn et al., 2004, Oñate et al., 2004). Computational domains are re-identified based on the particles followed by mesh generations. It has been shown that the PFEM is particularly suitable for modelling large deformation problems with free-surface evolutions (Oñate et al., 2011). So far, a series of challenging problems, in addition to landslides, in geomechanical and geotechnical problems have been tackled using the PFEM including, but are not limited to, ground excavation (Carbonell et al., 2010), granular flows (Lagrée et al., 2011, Zhang et al., 2013, Cante et al., 2014, Staron et al., 2014, Franci and Cremonesi, 2019), soil-structure interactions (Oñate et al., 2011, Monforte et al., 2017). Nevertheless, it is worth to note that a drawback associated with the PFEM for solving problems with history-dependent materials in geomechanics, or more generally solid mechanics, is the requirement of the variable mapping operation (Zhang et al., 2013). When new meshes are generated in the PFEM procedure, although information of displacements, velocities and accelerations is stored at mesh nodes and requires no mapping operation, field variables such as stresses, strains and other internal variables, for example those controlling the strain softening for sensitive clays (Zhang et al., 2017), have to be mapped from the old to the new integration points. Such a mapping operation inevitably leads to errors and increases complexity. To overcome this issue, the nodal integration method was recently introduced to the PFEM for geotechnical problems that the integrals are performed over smoothed domains rather than finite elements and all field variables are computed and stores at nodes (Zhang et al., 2018, Yuan et al., 2019). Franci et al. (2020) then explored the possibility of a nodal PFEM formulation for free-surface fluid dynamics problems. It has been shown that the PFEM with the nodal-integration technique not only circumvents the requirement of variable mappings as in the classical PFEM but also allows the use of low order elements, such as the 3-node triangle element, without volumetric locking and insensitivity to mesh distortion.

In this paper, the nodal-integration technique is implemented in the version of the PFEM developed in Zhang et al. (2013, 2017). Specifically, the nodal-integration technique is introduced to the dynamic finite element formulation in mathematical programming to form the N-FEM which is then incorporated in the PFEM framework to form the Nodal-based PFEM (N-PFEM). Compared to the existing PFEM with nodal-integration techniques in geomechanics in which an explicit integration scheme is used, the developed N-PFEM is based on implicit integration so that significantly larger time steps can be used in the simulation. This feature is of great importance for the modelling of cliff recession subject to weathering since the length of time to model is of some years. Additionally, as the finite element formulation developed in the presented N-PFEM is based on second-order cone programming, it inherits some unique merits of the FEM in mathematical programming that have been showcased in Krabbenhøft et al. (2007). Among them, a notable advantage for modelling landslide-induced cliff erosion rests with its convergence properties. Indeed, significant changes of stresses or strains may occur in just a very small time interval in the post-failure analysis of landslides. Whereas this critical change is likely to result in the nonconvergence of the standard Newton-Raphson based FEM, the adopted advanced optimisation algorithms still guaranteed the convergence regardless of whether the solved known states (e.g. the field variables at t_n) are close to the new unknown states (e.g. the field variables at t_{n+1}) (Zhang et al., 2014). The nodal integration also enables a more straightforward treatment of the cohesive-frictional contacts compared to the PFEM developed in Zhang et al. (2013, 2017). Last but not least, low-order elements such as the three node triangular element can be used in the developed version for tackling nearly incompressible problems while maintaining satisfactory accuracy which is not possible for the earlier PFEM version in Zhang et al. (2013, 2017) where six-node triangular elements are adopted for modelling geomechanical problems. To demonstrate the robustness and correctness of the developed N-PFEM, cliff recession under both weathering-limited and transport-limited conditions are considered. Comparisons between the simulation results from the N-PFEM and these from analytical approach and DEM modelling available in the literature are performed. Furthermore, the use of retaining wall for alleviating cliff recession subject to weathering is investigated using the N-PFEM with focus on the recession distance and the evolution of the resistance force from the retaining wall.

The paper is organised as follows. In Section 2, we present the formulations of the nodal-integration based finite element method (N-FEM). The merging of the N-FEM into the PFEM framework to form the N-PFEM is detailed in Section 3. Numerical benchmarks such as a block sliding on a rigid surface, cliff recession under uniform and non-uniform weathering conditions are illustrated in Sections 4 to 6 and the design of retaining wall structure to prevent cliff recession is discussed in Section 7. Conclusions are drawn in Section 8.

2. Nodal-integration based finite element method (N-FEM)

Before introducing the nodal-integration based particle finite element method (N-PFEM), the nodal-integration based finite element method (N-FEM) is formulated in this section, which is the core for solving the equations governing cliff erosion processes.

2.1 Governing equations

Considering a continuum medium with volume Ω, the momentum equations read

$$\begin{cases} \nabla^{\mathrm{T}}\boldsymbol{\sigma} + \boldsymbol{b} = \rho\dot{\boldsymbol{v}}, \text{ in } \Omega \\ \mathbf{N}^{\mathrm{T}}\boldsymbol{\sigma} = \boldsymbol{t}, \text{ on } \Gamma \end{cases} \tag{1}$$

where ∇ is the usual linear strain-displacement differential operator, $\boldsymbol{\sigma}$ is the stresses, $\mathbf{b}$ is the body forces, ρ is the density of the medium, $\boldsymbol{v}$ is the velocity with a superposed dot representing differentiation with respect to time, $\mathbf{N}$ is the matrix containing the unit outward normal to the boundary Γ and $\mathbf{t}$ is the traction. It can be discretised in time using the standard θ-method:

$$\begin{cases} \nabla^{\mathrm{T}}\left[\theta_1\boldsymbol{\sigma}_{\mathrm{n+1}} + (1-\theta_1)\boldsymbol{\sigma}_{\mathrm{n}}\right] + \boldsymbol{b} = \rho\dfrac{\boldsymbol{v}_{n+1} - \boldsymbol{v}_n}{\Delta t} \text{ and } \theta_2\boldsymbol{v}_{\mathrm{n+1}} + (1-\theta_2)\boldsymbol{v}_{\mathrm{n}} = \dfrac{\Delta\boldsymbol{u}}{\Delta t} \\ \mathbf{N}^{\mathrm{T}}\left[\theta_1\boldsymbol{\sigma}_{\mathrm{n+1}} + (1-\theta_1)\boldsymbol{\sigma}_{\mathrm{n}}\right] = \boldsymbol{t}_{\mathrm{n}}, \text{ on } \Gamma \end{cases} \tag{2}$$

where the subscripts n and n+1 refer to the known and unknown states in a typical time step, θ_1 and θ_2 are parameters taking values in [0, 1] and $\Delta\mathbf{u} = \mathbf{u}_{\mathrm{n+1}} - \mathbf{u}_{\mathrm{n}}$. The above equation can be reformulated as:

$$
\begin{cases}
\nabla^{\mathrm{T}}\boldsymbol{\sigma}_{\mathrm{n+1}} + \dfrac{(1-\theta_1)}{\theta_1}\nabla^{\mathrm{T}}\boldsymbol{\sigma}_{\mathrm{n}} + \hat{\mathbf{b}}_{\mathrm{n}} = \mathbf{r}_{\mathrm{n+1}} \\
\theta_1 \mathbf{N}^{\mathrm{T}}\boldsymbol{\sigma}_{\mathrm{n+1}} = \hat{\mathbf{t}}_{\mathrm{n}}
\end{cases}
\tag{3}
$$

where

$$
\begin{cases}
\hat{\mathbf{b}}_{\mathrm{n}} = \dfrac{\mathbf{b}}{\theta_1} + \dfrac{\rho \mathbf{v}_{\mathrm{n}}}{\theta_1 \Delta t \theta_2} \\
\mathbf{r}_{\mathrm{n+1}} = \dfrac{\rho}{\theta_1\theta_2}\dfrac{\Delta \mathbf{u}}{\Delta t^2} \\
\hat{\mathbf{t}}_{\mathrm{n}} = -\mathbf{N}^{\mathrm{T}}(1-\theta_1)\boldsymbol{\sigma}_{\mathrm{n}} + \mathbf{t}_{\mathrm{n}}
\end{cases}
\tag{4}
$$

Following Zhang et al. (2019a), the generalised Hellinger–Reissner variational principle for the discretised governing equations (3) and (4) with rate-independent materials reads:

$$
\begin{aligned}
\min_{\Delta \mathbf{u}} \max_{\boldsymbol{\sigma}_{\mathrm{n+1}},\, \boldsymbol{r}_{\mathrm{n+1}}} \quad & \int_\Omega \boldsymbol{\sigma}_{\mathrm{n+1}}^{\mathrm{T}} \nabla(\Delta \mathbf{u})\mathrm{d}\Omega + \frac{1-\theta_1}{\theta_1}\int_\Omega \boldsymbol{\sigma}_{\mathrm{n}}^{\mathrm{T}}\nabla\Delta\mathbf{u}_{\mathrm{n+1}}\mathrm{d}\Omega - \int_\Omega \hat{\boldsymbol{b}}_{\mathrm{n}}^{\mathrm{T}}\Delta\mathbf{u}_{\mathrm{n+1}}\mathrm{d}\Omega - \int_\Gamma \hat{\boldsymbol{t}}_{\mathrm{n}}^{\mathrm{T}}\Delta\mathbf{u}_{\mathrm{n+1}}\mathrm{d}\Gamma \\
& -\int_\Omega \frac{1}{2}(\Delta\boldsymbol{\sigma}_{\mathrm{n+1}})^{\mathrm{T}}\mathbb{C}(\Delta\boldsymbol{\sigma}_{\mathrm{n+1}})\mathrm{d}\Omega - \frac{1}{2}\Delta t^2\int_\Omega \boldsymbol{r}_{\mathrm{n+1}}^{\mathrm{T}}\hat{\rho}^{-1}\boldsymbol{r}_{\mathrm{n+1}}\mathrm{d}\Omega + \int_\Omega \boldsymbol{r}_{\mathrm{n+1}}^{\mathrm{T}}\Delta\mathbf{u}_{\mathrm{n+1}}\mathrm{d}\Omega \\
\text{subject to } & F(\boldsymbol{\sigma}_{n+1}) \le 0
\end{aligned}
\tag{5}
$$

In the above mixed variational principle, displacements, stresses and inertial forces are independent fields. F is the yield function and $\hat{\rho} = \dfrac{\rho}{\theta_1\theta_2}$. $\mathbb{C}$ is the elastic compliance modulus that, for plane-strain cases, is in the form:

$$
\mathbb{C} = \frac{1+\upsilon}{E}\begin{bmatrix} 1-\upsilon & -\upsilon & 0 \\ -\upsilon & 1-\upsilon & 0 \\ 0 & 0 & 2 \end{bmatrix}
\tag{6}
$$

where E and υ are elastic modulus and Poisson’s ratio, respectively. Its validity has been proved in Zhang et al. (2013, 2019a), and interested reader are referred to these references for details.

2.2 FEM with the nodal-integration technique

The discrete form of program (5) needs to be derived by using spatial discretisation methods. In the paper, the nodal-integration based finite element technique is adopted. By first using the standard finite element discretisation, we have:

$$\mathbf{u} \approx \mathbf{N}_{\mathrm{u}}\hat{\mathbf{u}} \tag{7}$$

where $\hat{\mathbf{u}}$ is a vector consisting of displacement at mesh nodes and $\mathbf{N}_{\mathrm{u}}$ is a matrix of shape functions. Following the classic FEM, the strain field is then approximated as:

$$\boldsymbol{\varepsilon} = \mathbf{B}_{\mathrm{u}}\hat{\mathbf{u}} \tag{8}$$

where $\mathbf{B}_{\mathrm{u}} = \nabla\mathbf{N}_{\mathrm{u}}$ is the strain-displacement matrix. Contrary to the standard FEM that integration is performed over finite elements, the integration in the proposed method is operated on cells. As shown in Fig.1, a cell (also called a smoothing domain) is a “non-overlap” and “no-gap” domain associated with each mesh node, for example, the cell Ω_k^s associated with the *k*th node (the red zone in Fig. 1) that covers several one-third of adjacent elements of a node *k*. The coloured polygon is bounded by multiple straight boundary segments which connect the midpoint of an edge to a centroid of the triangular elements. Consequently, the strain in the *k*th cell is the weighted average of the strain (or called smoothed strained) of all the one-third adjacent elements of node *k* (Zhang et al., 2018, Yuan et al., 2019, Franci et al., 2020)

$$\bar{\varepsilon}_k = \int_{\Omega_k^s} \Phi_k(\mathbf{x})\boldsymbol{\varepsilon}(\mathbf{x})\mathrm{d}\Omega = \int_{\Omega_k^s} \Phi_k(\mathbf{x})\mathbf{B}_{\mathrm{u}}\hat{\mathbf{u}}\mathrm{d}\Omega \tag{9}$$

where $\Phi_k(\mathbf{x})$ is the smoothing function in the form (Liu et al., 2009, Liu and Trung, 2010):

$$\Phi_k(\mathbf{x}) = \begin{cases} 1/A_k^s, & \mathbf{x} \in \Omega_k^s \\ 0, & \mathbf{x} \notin \Omega_k^s \end{cases} \tag{10}$$

in which A_k^s is the area of the smoothing domain Ω_k^s.

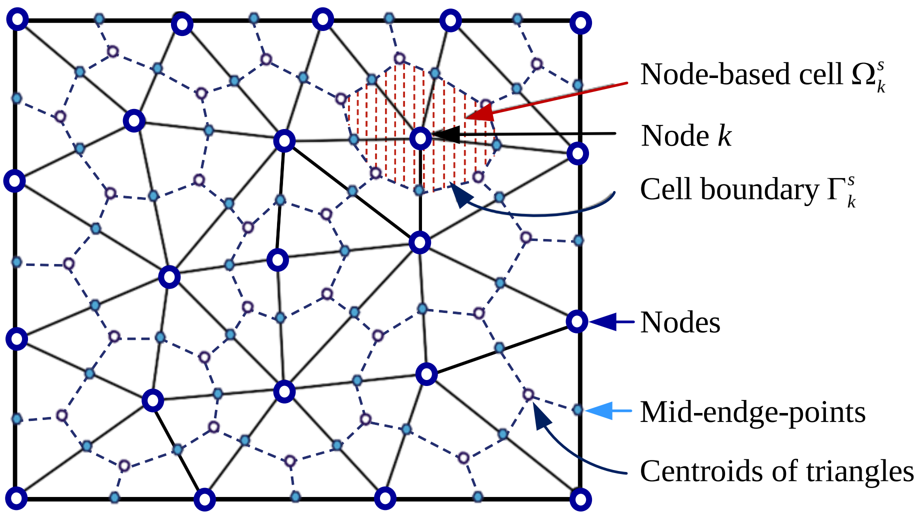

Fig. 1. Node-based cells (also called smoothing domains) based on given triangle mesh.

As demonstrated in Fig.1, the cell Ω_k^s is comprised of N_s sub-domains that are one-third of the triangular elements adjacent to node k. For the linear triangular element, the strain is constant inside the elements. Therefore, substituting Eq. (10) into (9), the smoothed strain $\bar{\boldsymbol{\varepsilon}}_k$ is simply:

$$\bar{\boldsymbol{\varepsilon}}_k = \frac{1}{A_k^s}\sum_{i=1}^{N_s}\frac{1}{3}A_i^e\boldsymbol{\varepsilon}_i^e = \frac{1}{A_k^s}\sum_{i=1}^{N_s}\frac{1}{3}A_i^e\mathbf{B}_i^e\hat{\mathbf{u}}_i^e \tag{11}$$

where i is the element number and $\mathrm{A}_i^e, \boldsymbol{\varepsilon}_i^e, \mathbf{B}_i^e$ and $\hat{\mathbf{u}}_i^e$ are the area, the strain, the strain gradient matrix and the displacement of the ith triangular element, respectively. For simplicity, the smoothed strain on the cell Ω_k^s is written as:

$$\bar{\boldsymbol{\varepsilon}}_k = \bar{\mathbf{B}}_k \hat{\mathbf{u}}_k \quad \text{with} \quad \bar{\mathbf{B}}_k = \frac{1}{\mathrm{A}_k^s} \sum_{i=1}^{N_s} \frac{1}{3} \mathrm{A}_i^e \mathbf{B}_i^e \tag{12}$$

where $\hat{\mathbf{u}}_k$ is the nodes' displacement of the cell k. Thus for each cell, the strain increment

$$\Delta\boldsymbol{\varepsilon} = \nabla\left(\Delta\mathbf{u}\right) = \bar{\mathbf{B}}\hat{\mathbf{u}} \tag{13}$$

where $\bar{\mathbf{B}}$ consists of the smoothed strain-displacement matrix as shown in Eq (12).

As the mixed variational principle is adopted, state variables such as the displacement, the stress and the dynamic force have to be interpolated independently. Herein for each cell, we have

$$\boldsymbol{\sigma} \approx \mathbf{N}_\sigma \bar{\boldsymbol{\sigma}} \tag{14}$$

where $\bar{\boldsymbol{\sigma}}$ is the smoothed stress and $\mathbf{N}_\sigma$ is the shape function matrix which are in fact identity matrices since the linear approximation is made for the displacement field, and

$$\boldsymbol{r} \approx \mathbf{N}_\mathrm{r} \tilde{\boldsymbol{r}} \tag{15}$$

where $\tilde{\boldsymbol{r}}$ is the dynamic force applied on the nodes, and $\mathbf{N}_r$ is the corresponding shape function matrix. Note that the displacement approximation for elements in the approach is the same as in the classic FEM and therefore shape function matrix for force vectors is constructed in the same way as in the classic FEM.

Substituting the approximations in (13), (14) and (15) into the spatially continuous variational principle (5) results in the fully discrete problem:

$$\begin{aligned}&\min_{\Delta\hat{\mathbf{u}}}\ \max_{\bar{\boldsymbol{\sigma}}_{\mathrm{n+1}},\, \bar{\boldsymbol{r}}_{\mathrm{n+1}}}\quad \Delta\hat{\mathbf{u}}^{\mathrm{T}}\mathbf{B}^{\mathrm{T}}\bar{\boldsymbol{\sigma}}_{\mathrm{n+1}} - \frac{1}{2}\Delta\bar{\boldsymbol{\sigma}}_{\mathrm{n+1}}^{\mathrm{T}}\mathbf{C}\Delta\bar{\boldsymbol{\sigma}}_{\mathrm{n+1}} - \frac{1}{2}\Delta t^{2}\tilde{\boldsymbol{r}}_{\mathrm{n+1}}^{\mathrm{T}}\mathbf{D}_{r}\tilde{\boldsymbol{r}}_{\mathrm{n+1}} + \Delta\hat{\boldsymbol{u}}_{n+1}^{\mathrm{T}}\mathbf{A}^{\mathrm{T}}\tilde{\boldsymbol{r}}_{\mathrm{n+1}} - \Delta\hat{\mathbf{u}}^{\mathrm{T}}\tilde{\mathbf{f}}\\ &\text{subject to } F\left(\bar{\boldsymbol{\sigma}}_{\mathrm{n+1}}\right) \le 0\end{aligned} \tag{16}$$

where

$$\begin{aligned}&\mathbf{B}^{\mathrm{T}} = \int_{\Omega}(\bar{\mathbf{B}})^{\mathrm{T}}\mathbf{N}_{\sigma}\mathrm{d}\Omega, \qquad \mathbf{C} = \int_{\Omega}\mathbf{N}_{\sigma}^{\mathrm{T}}\mathbb{C}\mathbf{N}_{\sigma}\mathrm{d}\Omega,\\ &\mathbf{D}_{r} = \int_{\Omega}(\mathbf{N}_{u})^{\mathrm{T}}\hat{\rho}^{-1}\mathbf{N}_{\mathrm{u}}\mathrm{d}\Omega,\ \mathbf{A}^{\mathrm{T}} = \int_{\Omega}(\mathbf{N}_{\mathrm{u}})^{\mathrm{T}}\mathbf{N}_{\mathrm{u}}\mathrm{d}\Omega,\\ &\tilde{\mathbf{f}} = \int_{\Omega}\mathbf{N}_{\mathrm{u}}^{\mathrm{T}}\hat{\mathbf{b}}_{\mathrm{n}}\mathbf{N}_{\sigma}\mathrm{d}\Omega + \int_{\Gamma}\mathbf{N}_{\mathrm{u}}^{\mathrm{T}}\hat{\mathbf{t}}_{\mathrm{n}}\mathrm{d}\Gamma - \frac{1-\theta_{1}}{\theta_{1}}\bar{\mathbf{B}}^{\mathrm{T}}\bar{\boldsymbol{\sigma}}_{\mathrm{n}}\end{aligned} \tag{17}$$

It is noteworthy that all integration operations for equations in (17) are carried out on cells using the nodal-integration technique rather than on finite elements using Gauss integration technique. Thus information on all the variable states, such as displacements, velocities, strains, stresses, etc., is stored on mesh nodes. A proper treatment with boundaries in the numerical model is essential. Inspired by the recently proposed framework for the discrete element method (Krabbenhoft et al., 2012, Meng et al., 2018, 2019a), the purely frictional and cohesive-frictional contact interfaces are accounted for. As indicated in Fig. 2, frictional/cohesive-frictional behaviour is considered for yellow smoothing domains in contact with the boundary while red smoothing domains have potential contacts. To prevent the penetration into the boundary, the following non-penetration condition is employed:

$$\begin{aligned}&g^{I} = g_{0}^{I} + \left(\Delta\hat{\mathbf{u}}^{I}\right)^{\mathrm{T}}\boldsymbol{n}^{I} \ge 0\\ &p^{I}g^{I} = 0\end{aligned} \tag{18}$$

where $\Delta\hat{\mathbf{u}}^I$ is the displacement increments of the node at contact I, $\boldsymbol{n}^I$ is the outward normal vector of the boundary, p^I is the contact force from the boundary, g_0^I is the initial gap and g^I is the gap at the next step.

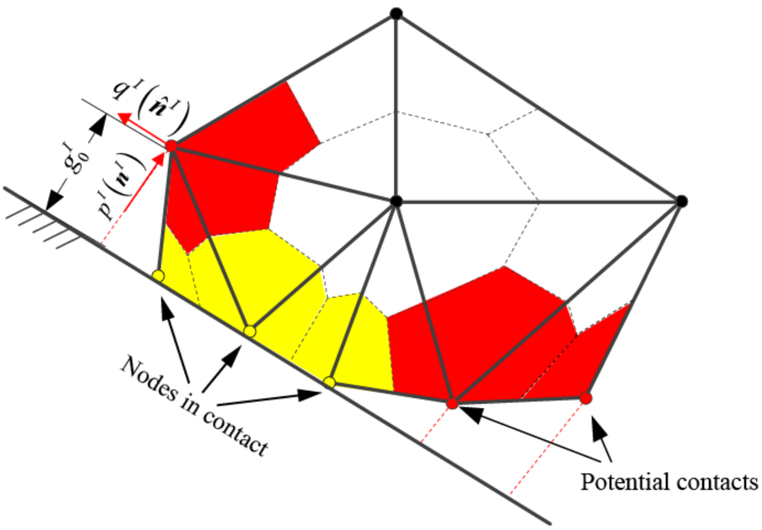

Fig. 2. The boundary condition for a deformable body. Smoothing domains are shown with dash lines. Smoothing domains with frictional/cohesive-frictional interfaces are coloured in yellow.

Following the approach in Meng et al. (2019b), the condition (18) can be enforced into the principle leading to:

$$
\begin{aligned}
&\min_{\Delta\hat{\mathbf{u}}} \max_{\bar{\sigma}_{n+1},\, \bar{\boldsymbol{r}}_{n+1},\, \boldsymbol{p},\, \boldsymbol{q}} \quad \Delta\hat{\mathbf{u}}^{\mathrm{T}}\mathbf{B}^{\mathrm{T}}\bar{\boldsymbol{\sigma}}_{n+1} - \frac{1}{2}\Delta\bar{\boldsymbol{\sigma}}_{n+1}^{\mathrm{T}}\mathbf{C}\Delta\bar{\boldsymbol{\sigma}}_{n+1} - \frac{1}{2}\Delta t^2\tilde{\boldsymbol{r}}_{n+1}^{\mathrm{T}}\mathbf{D}_r\tilde{\boldsymbol{r}}_{n+1} + \Delta\hat{\boldsymbol{u}}_{n+1}^{\mathrm{T}}\mathbf{A}^{\mathrm{T}}\tilde{\boldsymbol{r}}_{n+1} - \Delta\hat{\mathbf{u}}^{\mathrm{T}}\tilde{\mathbf{f}} \\
&\qquad\qquad - \Delta\hat{\mathbf{u}}^{\mathrm{T}}\left(\boldsymbol{n}\boldsymbol{p} + \hat{\boldsymbol{n}}\boldsymbol{q}\right) - \sum_{I=1}^{N_b} g_0^I p^I \\
&\text{subject to} \qquad F\left(\bar{\boldsymbol{\sigma}}_{n+1}\right) \le 0 \\
&\qquad\qquad\qquad F_b\left(\boldsymbol{p},\ \boldsymbol{q}\right) \le 0
\end{aligned} \tag{19}
$$

where N_b is the number of boundary contacts, the normal and tangential vectors of the boundaries are collected in $\boldsymbol{n}$ and $\hat{\boldsymbol{n}}$, respectively, contact forces in the normal and tangential directions are organised into vectors $\boldsymbol{p}$ and $\boldsymbol{q}$, respectively, and shear strength for boundary contacts is considered with a constraint (i.e., $F_b(\boldsymbol{p}, \boldsymbol{q}) \le 0$) as:

$$\begin{cases} |\boldsymbol{q}| \le \mu \boldsymbol{p}, & \text{purely frictional interfaces} \\ |\boldsymbol{q}| \le \mu \boldsymbol{p} + c\boldsymbol{A}, & \text{cohesive-frictional interfaces} \end{cases} \tag{20}$$

where μ is the friction coefficient, c is the cohesion of the shear strength and $\boldsymbol{A}$ is the vector collecting all cohesive interfaces' area. Principle (19) is thus the discretised optimisation problem for the nodal-integration based finite element method with contacts (N-FEM). Following the procedure in the appendix, principle (19) can be cast into a standard second-order cone program. Thus, efficient standard second-order cone programming solvers can be employed.

3. Implementation of the nodal-integration based PFEM (N-PFEM)

Similar to the idea of the PFEM for geomechanics problems in Zhang et al. (2013), the key feature of the modelling procedure of the N-PFEM is that nodes are viewed as free "particles" that can move and even separate from the domain to which they originally belong. On the basis of the particle distribution, the computational domain is re-identified and discretised in space at each time step and then the governing equations are resolved. Nevertheless, compared to the classical PFEM, the proposed N-PFEM does not require the operation of variable mapping when it is used for solving geomechanical problems. This is owing to the fact that has been indicated in Section 2.2 that information of all field variables is stored on mesh nodes and the nodal integration is performed. Briefly, the computational cycle of the N-PFEM for a typical time interval is as follows (see also Fig. 3):

1. The computational domain is represented by a cloud of particles at time t_n.

2. The alpha-shape technique is adopted to identify the boundary of the computational domain and then triangle meshes are generated based on the particles and identified boundary;

3. Cells (e.g. smoothing domains) are constructed according to the topology of the triangle meshes, on which the N-FEM is resolved to obtain the state of field variables at t_{n+1};

4. Update the position of the particles to form the new cloud of particles;

5. Loop the above process over all time steps.

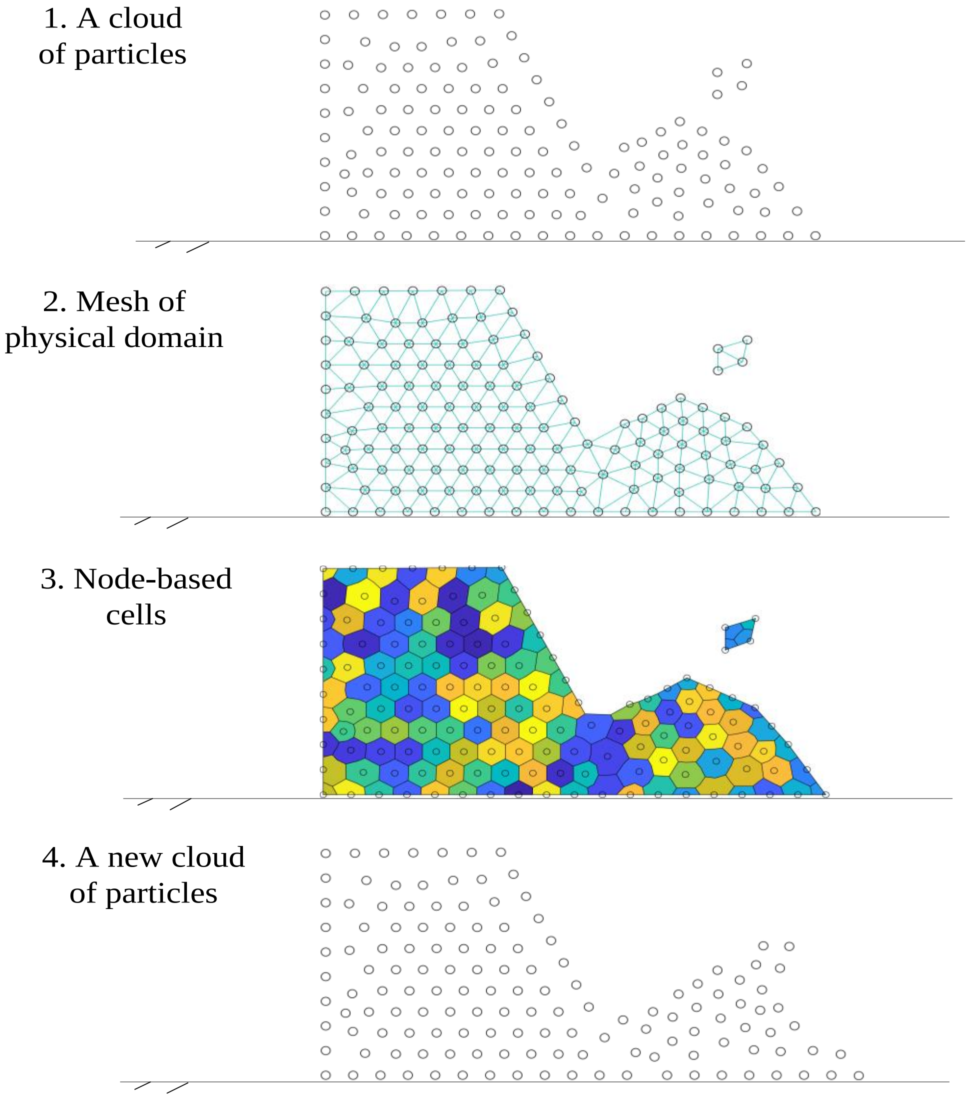

Fig. 3. Computational cycle of the N-PFEM

4. Validation on a sliding block

For the purpose of verification, the developed approach is adopted to simulate a block (2 m long and 1 m high) that slides on a slope as shown in Fig. 4 (a). Model parameters for the simulation include the unit weight of the block of 20 kN/m^3 and the inclined slope angle of 45° and 60°. The time step used in the simulation is 0.01 s, which is sufficiently small to obtain convergence. Both the Young's modulus and the strength of the block are set to be sufficiently large so that the block behaves nearly as a rigid body. Both purely frictional and cohesive-frictional interfaces between the block and the inclined slope were considered. The frictional angle for the contact interface between block and plane was 20° with three different values of cohesion considered: 0 kPa, 1 kPa and 10 kPa. The analytical solution of the block sliding distance S can be derived from first principles:

$$S = 0.5(g\sin(\beta) - g\cos(\beta)\mu - cA/m)t^2 \tag{21}$$

where β is an angle of slope inclination, μ is the interface frictional coefficient (tan20°), g is the gravitational acceleration (10 m/s^2), t is the sliding time, c is the interface cohesion, A is the interface area (2 m^2) and m is the block mass (4×10^3 kg).

The simulation results and the analytical solutions of the displacement versus time are shown in Fig. 4(b): excellent agreement of the simulation results with the analytical solution can be observed.

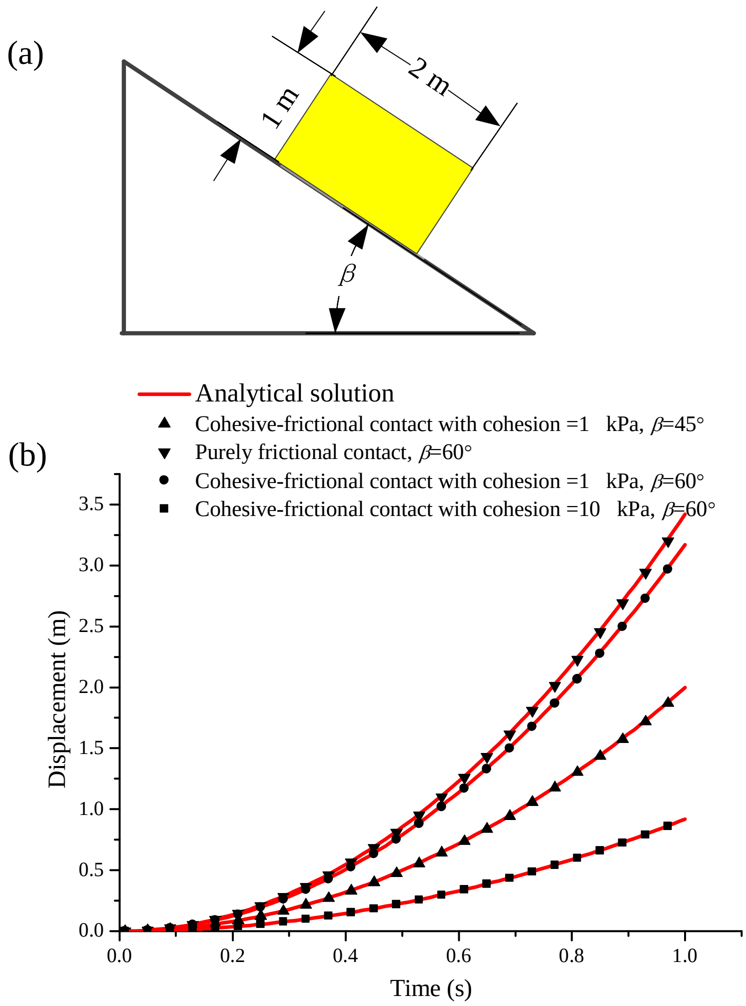

Fig. 4. The sliding of a block: (a) geometric model and (b) comparison between numerical and analytical solutions.

5. Uniform weathering: N-PFEM Versus Limit Analysis

A vertical uniform slope subjected to the uniform weathering that has been studied using the limit analysis method in Utili and Crosta (2011a) is here considered. The vertical slope is 40 m high with a unit weight of 20 kN/m^3. Three different meshes, namely a coarse one (4876 elements), a fine one

(10950 elements) and a very fine one (30276 elements) are used to discretise the vertical slope as illustrated in Fig. 5.

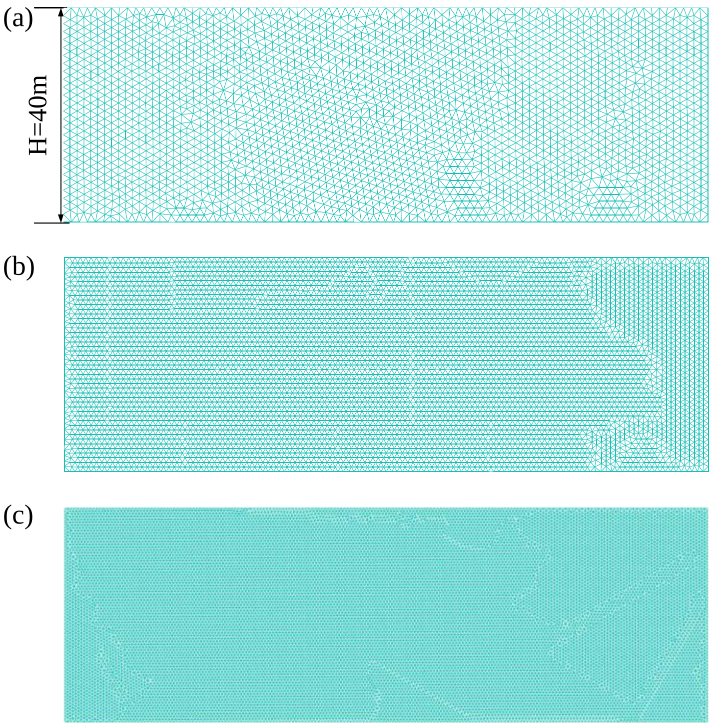

Fig. 5 Uniform weathering model with (a) a coarse mesh, (b) a fine mesh and (c) a very fine mesh.

Weathering causes a decrease of the strength of the slope materials over time (Gupta and Rao, 2000, Gullà et al., 2006, Tran et al., 2019). Kimmance (1988) reported experimental data of weathering of granites as shown in Fig. 6(a). It is evident that weathering causes a reduction mainly of cohesion and to a much lesser extent of the friction angle. The same phenomenon is observed for hard soils such as cemented sands (Wang and Leung, 2008) as shown in Fig. 6(b). Here, we assumed a weathering induced cohesion only decrease (constant friction) for sake of comparison with the main cliff retreat scenario presented in Utili and Crosta (2011a) in section 3.3. Following Utili and Crosta

(2011a) the initial cohesion of the geo-material is set to 500 kPa and a constant frictional angle of 34˚, is adopted (Utili and Crosta, 2011a).

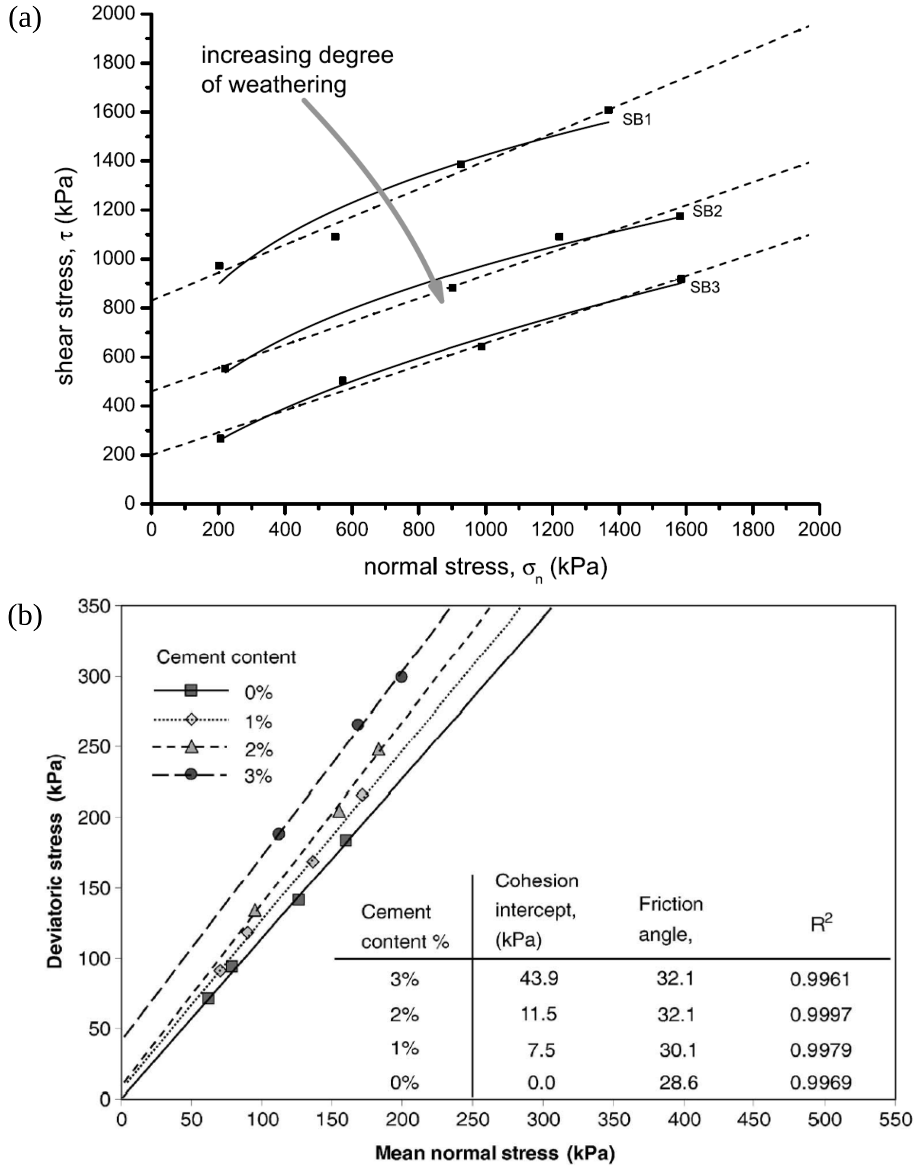

Fig. 6. Mechanical degradation of geo-materials due to weathering: (a) granites (after Kimmance, 1988) and (b) cemented sand (after Wang and Leung, 2008). Different weathered granite samples have been adopted for testing and indicated with SB1, SB2 and SB3 in Fig 6(a). SB1, SB2 and SB3 samples represent weak brownish grey granites, moderately to highly altered granites and highly altered granites, respectively.

The condition of strong erosion (also called weathering-limited erosion) is here assumed. This means that after each slope failure the landslide debris is removed from the model. The cohesion of the geo-materials is decreased by small steps of by 0.5 kPa. Slope failure occurs once a shear band has developed from the slope toe all the way to the slope upper horizontal level as shown in Fig.7. In this study several successive failure events take place, so it is important to identify slope failures in a consistent way for all the failures taking place. Common criteria in the literature are in terms of loss of static equilibrated solution for the failing mass or the achievement of a threshold of strain or displacement at some reference points in the slope (Lane & Griffiths, 1999). Here for reasons of ease of computation, the horizontal displacement of the slope crest d_{crest}, normalised by the slope height, was considered: I= d_{crest}/H. The threshold value for failure assumed in our simulations was $I_{\mathrm{failure}} = 3.5\times10^{-3}$. After a slope failure is identified, the failed slope mass is deleted to replicate strong erosion (the marked nodes in Fig. 7). Mesh convergence of the evolution processes produced by the proposed method is examined and the simulation results are also compared to those from limit analysis in Utili and Crosta (2011a). Fig. 8 shows the relationship between the normalised cohesion $c/(\gamma \mathrm{H})$ and the crest retreat normalised by slope height CR/H, where c is the cohesion, γ is the unit weight, H is the slope height and CR is the crest retreat distance. The steps shown in the figure result from a sequence of discrete landslide events. Each landslide event leads to a finite retreat of cliff, corresponding to horizontal lines. Between landslide events the slope is stable with the ground strength parameters progressively being degraded due to weathering captured by the vertical lines in Fig. 8.

A satisfactory agreement between the results from the proposed method and the limit analysis solutions from Utili and Crosta (2011a) can be observed for the first four failure mechanisms which are enough to track how the cliff profile evolves due to the weathering action. The little discrepancy between two methods is to be attributed to the following factors: 1) in the limit analysis model of

(Utili and Crosta, 2011a) a logarithmic spiral failure surface is assumed, whereas in our approach the failure surface is obtained as result of the simulations without any predefined assumption on its shape; and 2) some approximation in identifying the failure surface in our approach due to the FEM space discretization as shown in Fig. 7.

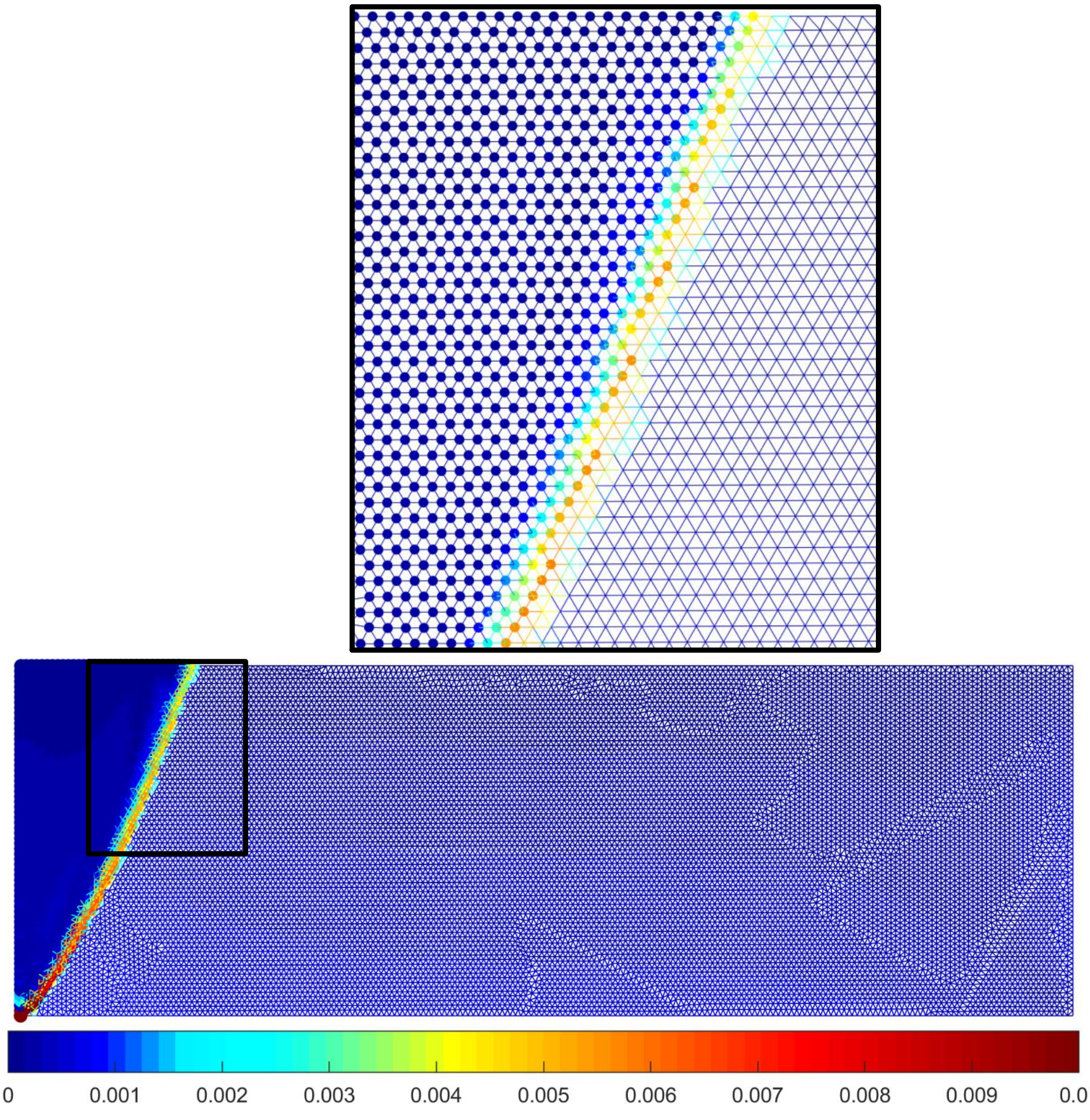

Fig. 7. Shear band at the onset of the first failure. Colours are proportional to equivalent plastic strain increment. The mesh marked with nodes is considered as failure mass.

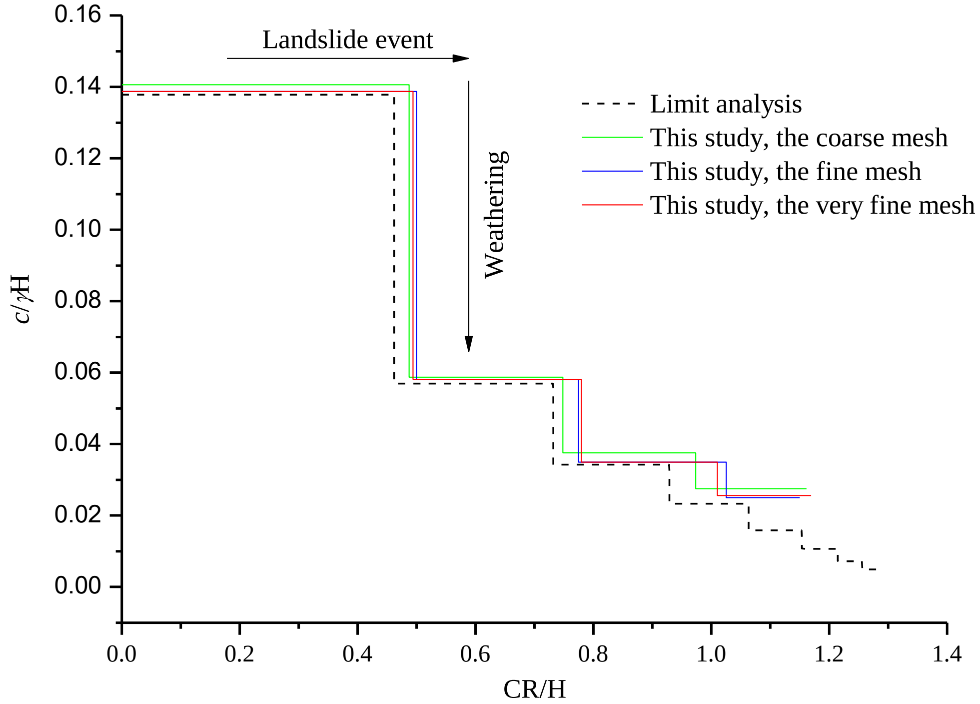

Fig. 8. Uniform weathering results (dimensionless normalised cohesion and the crest retreat).

With regard to the dependence of the results from mesh size, the predicted cliff retreat from the fine mesh and the very fine mesh are identical for all practical purposes. However the value of cohesion at failure is not the only feature to check since the geometry of the failure mechanism is also important. The slope profiles after the fourth failure predicted by the proposed method using different meshes are illustrated in Fig. 9. It is evident that the shapes of the slope profile left are very similar. Thus the fine mesh will be used to simulate the case of the non-uniform degradation in the following sections for the sake of computational efficiency.

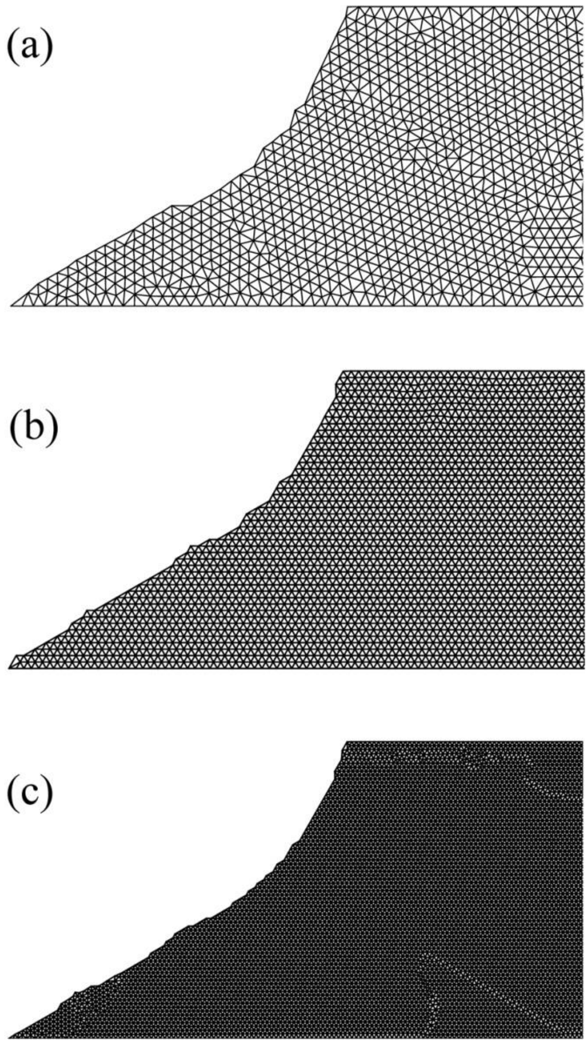

Fig. 9. The slope shape after the fourth failure subject to uniform weathering with (a) a coarse mesh, (b) a fine mesh and (c) a very fine mesh.

6. Non-uniform degradation

In this section, a more realistic weathering scenario, namely the non-uniform weathering over time and space, is considered. Additionally, the transport-limited condition is here investigated. The condition implies that the debris accumulates at the toe of the slope after each landslide event (Utili and Crosta, 2011b). Therefore both the onset of failure and the movement of the debris need to be correctly simulated for the model to capture the evolution of the cliff investigated.

In light of field hardness tests taken at different depth from the exposed surface of a cliff subject to weathering (Yokota and Iwamatsu, 2000), a weathering front parallel to the exposed surfaces moving inwards at a constant rate is here assumed as shown in Fig. 10. The weathering depth is $W_{front}= v_{front} \times t_{real}$ where v_{front} is the speed of the weathering front and t_{real} is the physical time. The damage index D is used to quantify the degradation of the cliff subjected to weathering. Specifically, for intact rocks, the damage index is D=0, while we have D=1 if the rocks are fully weathered. Currently, data related to quantitative descriptions on strength degradation within natural slopes induced by weathering are scanty. Thus, cohesion is reduced to zero for fully weathered geo-materials to validate the approach against the predictions of cliff evolution from Discrete Element simulations reported in Utili and Crosta (2011b). The decrease of cohesion over time is given by:

$$c(\mathrm{t})=c \times (1 - \mathrm{D}) \tag{21}$$

W_D as shown in Fig. 10 is the width of partially weathered zone, in which the damage index D changes linearly from 1 to 0. W_D is given by:

$$W_D = v_{front}/\ v_D \tag{22}$$

where v_D is the damage rate, i.e. the increment of D over time. In the simulations, the damage index inside the slope is prescribed as shown in Fig. 10. The shear strength inside the slope can be determined from Eq. (21).

Since the spatial distribution of weathering changes over time, it is necessary to explicitly assume an initial condition to simulate the progression of degradation with time unlike the case of uniform degradation. The initial condition assumed at t_0, was that of unweathered material: D=0 throughout the whole slope. This assumption supposes the existence of a time when the cliff was characterised by a uniform strength which could be thought as the time of formation of the cliff: for instance, the formation of a scarp or a hillslope because of a deep-seated landslide, a series of rapid displacements along a specific plane (e.g. fault) or erosion and deposition of river terraces. This is also the standard assumption in the Fisher-Lehmann and Bakker-Le Heux models.

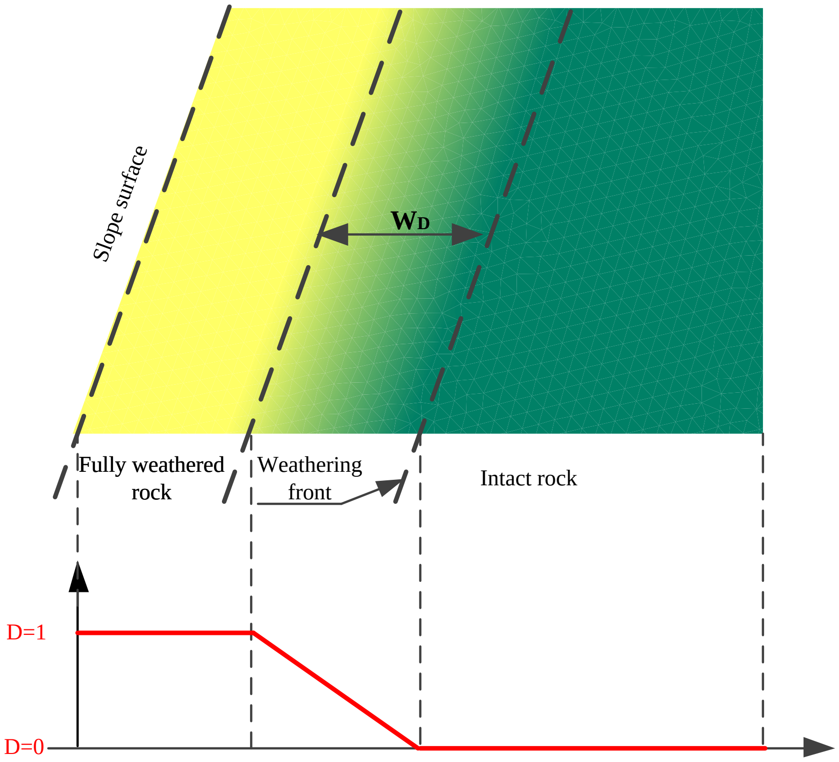

Fig. 10. The weathering process within the cliff.

Weathering is usually very slow. Therefore the weathering rate needs to be speeded up to run the simulations in a feasible computation time as indicated in Utili and Crosta (2011b). This means that a fictitious simulation time needs to be employed. The ratio between the fictitious time in the simulation t_{sim} and the real time t_{real} is:

$$t_{real} = t_{sim} \times \kappa \tag{23}$$

where κ is the speedup ratio defined as the ratio of the physical time to the simulation time.

The cliff model considered in Utili and Nova (2008) and Utili and Crosta (2011a) is used in this study which is also shown in Fig. 12 (a). The velocity of the weathering front is v_{front} =0.01 m/year and W_D is 2 m. The material parameters are the same as these for the case of uniform weathering except that the non-associated plastic flow with a null dilation angle is assumed for the geo-material in this section. To calibrate the speedup ratio, κ is set to 0.50×10^{10}, 1.00×10^{10} and 1.58×10^{10} corresponding to a speedup velocity of the weathering front of 1.59, 3.17 and 5.00 m/s, respectively. Note that as soon as dynamic motion in any point in the slope is identified, weathering is stopped and the speed up ratio is set to unity, i.e. the real time coincides with the simulation time, for the whole duration of the dynamic motion until the landslide body stops its motion. Then, once quasi-static conditions are resumed, weathering scaling is also resumed with the speed up ratio set to its original value until the next failure occurs. One simulation, consisting of a sequence of discrete landslide events and slow weathering process, required around 62.6 hours to complete.

The results of the simulation in terms of normalised crest retreat versus propagation distance of the Weathering Front (WF) for WF/H<0.4 are shown in Fig. 11. The crest retreats obtained for κ = 0.50×10^{10} and κ= 1.00×10^{10} are in a good agreement, indicating that the speedup ratio κ= 1.00×10^{10} is sufficiently small not to unduly affect the results. This ratio was therefore adopted in all subsequent simulations.

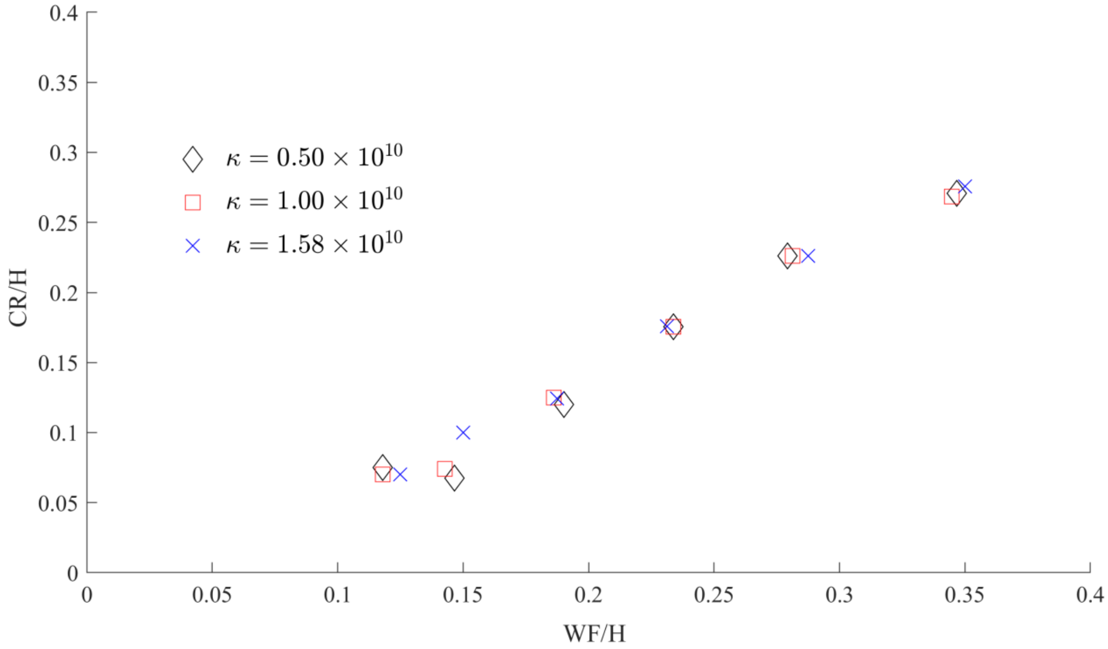

Fig. 11. Dimensionless crest retreat versus weathering front under different speedup ratios. WF is the propagation distance of the weathering front.

The predicted cliff profiles over time are shown in Figs. 12 (b)-(i) with the associated weathering fronts plotted in Fig.13. As it can be seen in Fig.13 (i), at the end of the cliff geometric evolution, most of the slope is fully weathered and the final angle of repose of the scree made of debris is about 30° over the horizontal. In Fig. 12, the debris materials are depicted in blue and the so-called non-displaced undisturbed zone is in red. It emerges that the free cliff front (e.g. the surface from the crest of the slope to the rear of the accumulated debris) remains parallel to the original cliff surface which is represented by a dashed line. This phenomenon produced by the N-PFEM simulation confirms the assumption made by the Fisher-Lehmann model (Fisher, 1866, Lehmann, 1933), which is a classic geomorphologic model to predict the shape of the undisturbed zone of slopes subjected to weathering, that in a given time weathering produces an equal retreat of all parts of the exposed free face by the falling away of fine debris. Readers interested in the assumption of this geomorphologic model and the equation of the shape of the undisturbed zone are referred to Hutchinson (1998).

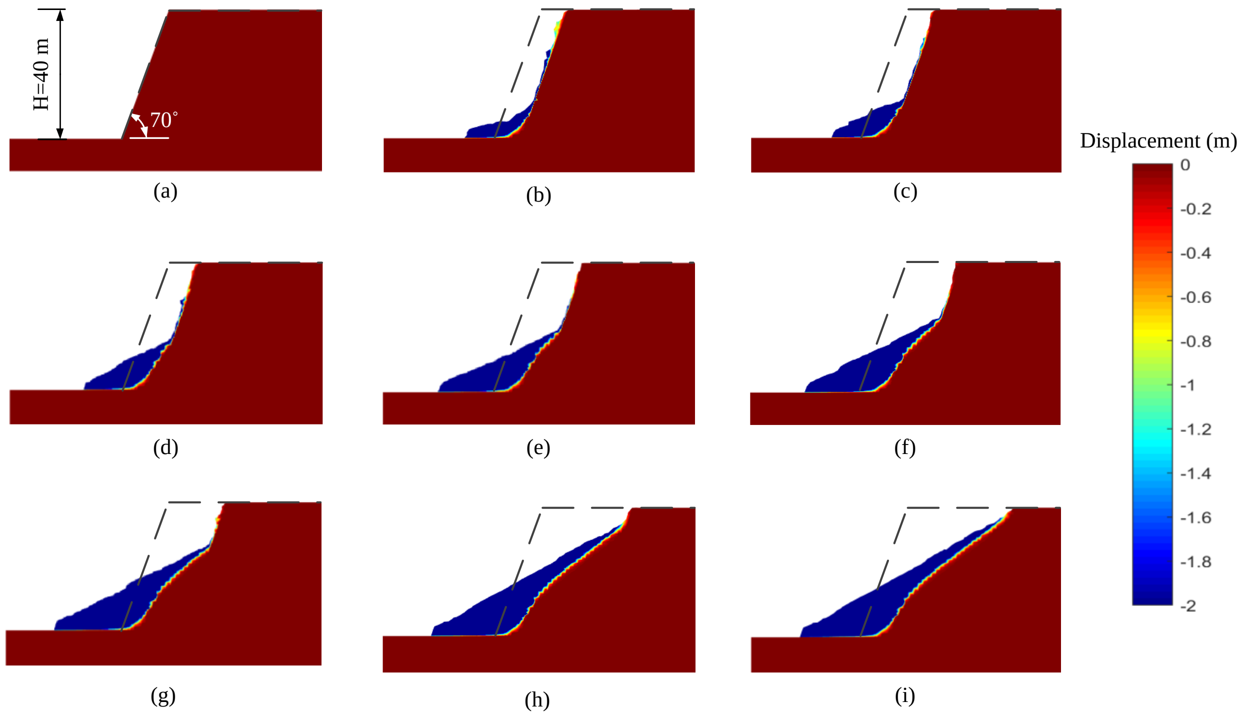

Fig. 12. The evolution of the slope subjected to weathering propagation at simulation time of (a) 0.0 s, (b) 1.5 s (c) 1.8 s, (d) 2.4 s (e) 3.3 s (f) 4.1 s (g) 5.4 s (h) 8.2 s and (i) 16.0 s. Colours are proportional to the accumulated horizontal displacement (m). The blue indicates the sliding mass while the undisturbed zone in the slope is indicated in red.

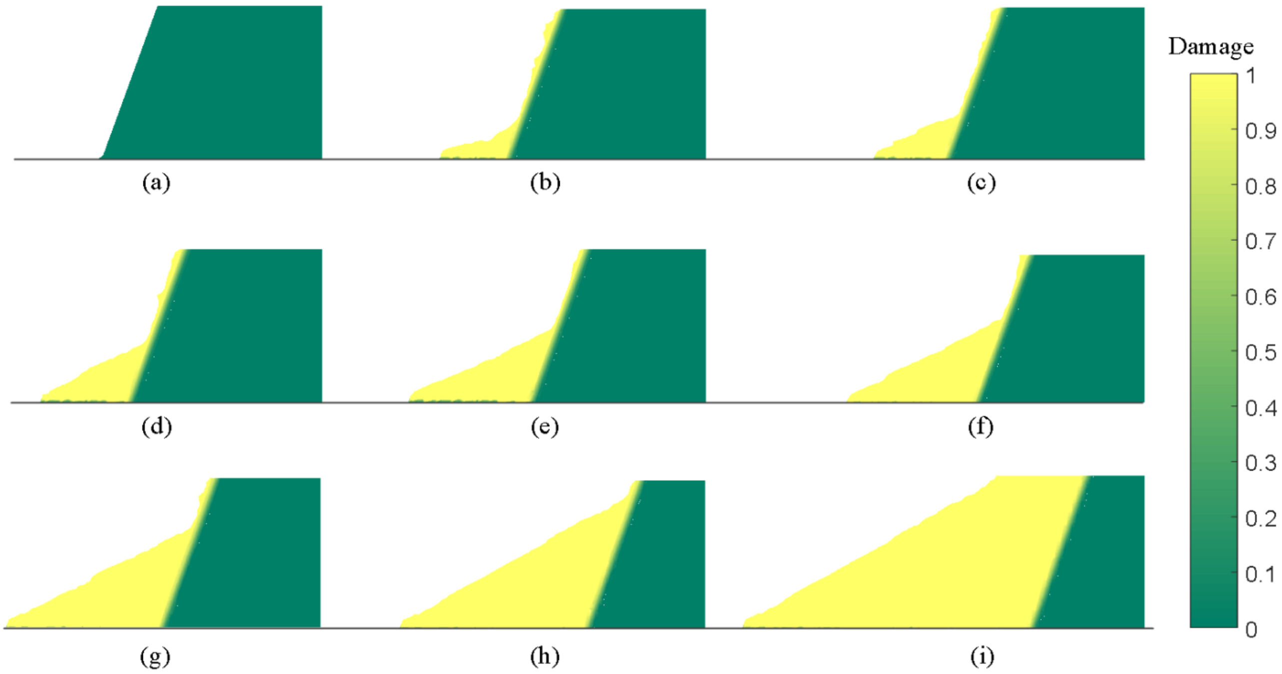

Fig. 13. The propagation of weathering front at simulation time of (a) 0.0 s, (b) 1.5 s (c) 1.8 s, (d) 2.4 s (e) 3.3 s (f) 4.1 s (g) 5.4 s (h) 8.2 s and (i) 16.0 s. Colours are proportional to the damage index, D. The green indicates the intact mass while the fully weathered materials are in yellow.

In Fig.14 the final deposit predicted by the N-PFEM method (Fig. 12 (i)) is compared to the DEM simulations in Utili and Crosta (2011b), yellow curves, and that from the Fisher-Lehmann geomorphologic model (Fisher, 1866, Lehmann, 1933). The results of the three methods broadly agree well with each other. It can be seen that the proposed N-PFEM and the DEM produce very similar results in terms of both the shape of the undisturbed zone and the slope profile. An advantage of the N-PFEM model over the DEM is that, as a continuum approach, it does not require the calibration process needed for the particle bond parameters of the DEM modelling.

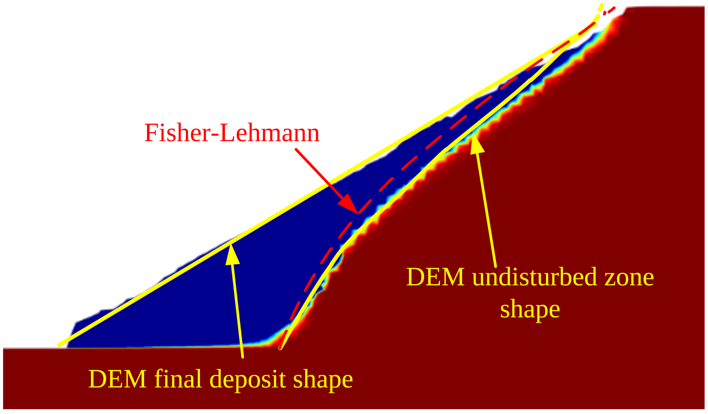

Fig.14. Final deposit of the slope derived from the N-PFEM, the DEM (Utili and Crosta, 2011b) and the Fisher-Lehmann model.

7. Retaining wall design

In order to prevent the cliff recession due to weathering induced landslides, one of the measures commonly taken in practical engineering is the construction of retaining wall structures. In this study, the performance of the retaining wall against weathering induced cliff failures is shown in Fig. 15. The higher the retaining wall, the safer the slope but the associated construction and maintenance costs will also be higher. Therefore, it is important to strike the right balance with respect to the wall construction costs. For this purpose, the performance of retaining wall with different heights (i.e. 0 m, 5 m, 10 m, 15 m, 20 m to 25 m) is investigated using the proposed N-PFEM. As a matter of fact, the retaining wall will eventually be degraded due to weathering in the very long term. In our simulations the rigid retaining wall is modelled as rough boundary condition. The parallel weathering model described for the non-uniform weathering case in section 6 was adopted together with the slope material parameters. A faster weathering rate is considered with v_{front} =0.1 m/year; W_D is 2 m and the speedup ratio κ is reduced to 1.00×10^9.

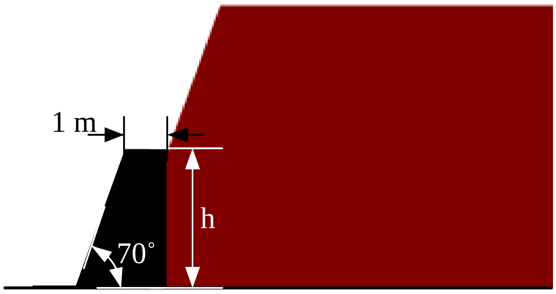

Fig.15. The numerical model with a retaining wall structure.

The evolution of the slope subjected to weathering is shown in Fig. 16 while the simulation results for the crest retreat over time are shown in Fig. 17 in which the height of the retaining wall is normalized by the height of the slope, h/H, and so does the distance of crest retreat (i.e. CR/H).

Fig. 17 indicates that the first crest retreat event occurs at about 57.1 years (simulation time = 1.5 s) regardless of the height of the retaining wall. There is also no clear difference on the crest retreat distance between different cases until the slope with the highest retaining wall reaches its final deposit profile at 199.8 years (simulation time = 6.3 s). The detached debris covers the whole retaining wall for the lower retaining wall structure (i.e. $h/H \leq 0.375$) implying that the effect of the retaining wall on the shape of the scree resting on the slope base is negligible. In addition, the crest retreat distances for these four cases are comparable. The slope with second highest retaining wall ($h/H=0.5$) reaches its final deposit profile at 255.3 years (simulation time = 8.05 s). At the final stage, the slopes with $h/H \geq 0.5$ has a much lower crest retreat while, for the cases with low retaining walls (i.e. $h/H \leq 0.375$), the effect of the retaining wall on the crest retreat is insignificant.

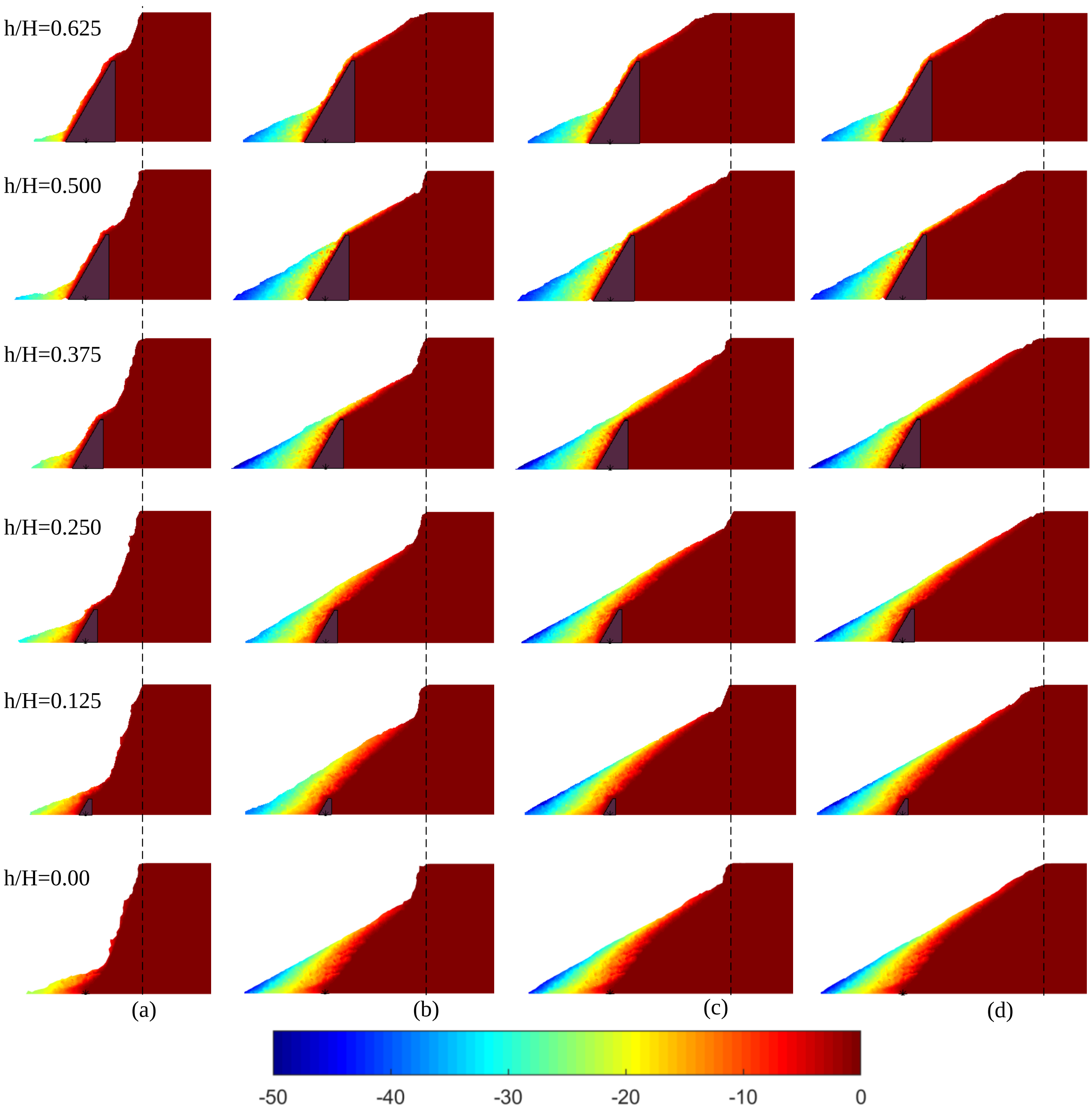

Fig. 16. Evolution of the cliff with different retaining wall heights at different simulation time instants: (a) 1.8 s, (b) 6.3 s, (c) 8.05 s and (d) 16.0 s. Colours are proportional to accumulated the horizontal displacement (m) and black dash lines indicate crest retreat of the cliff without the retaining wall.

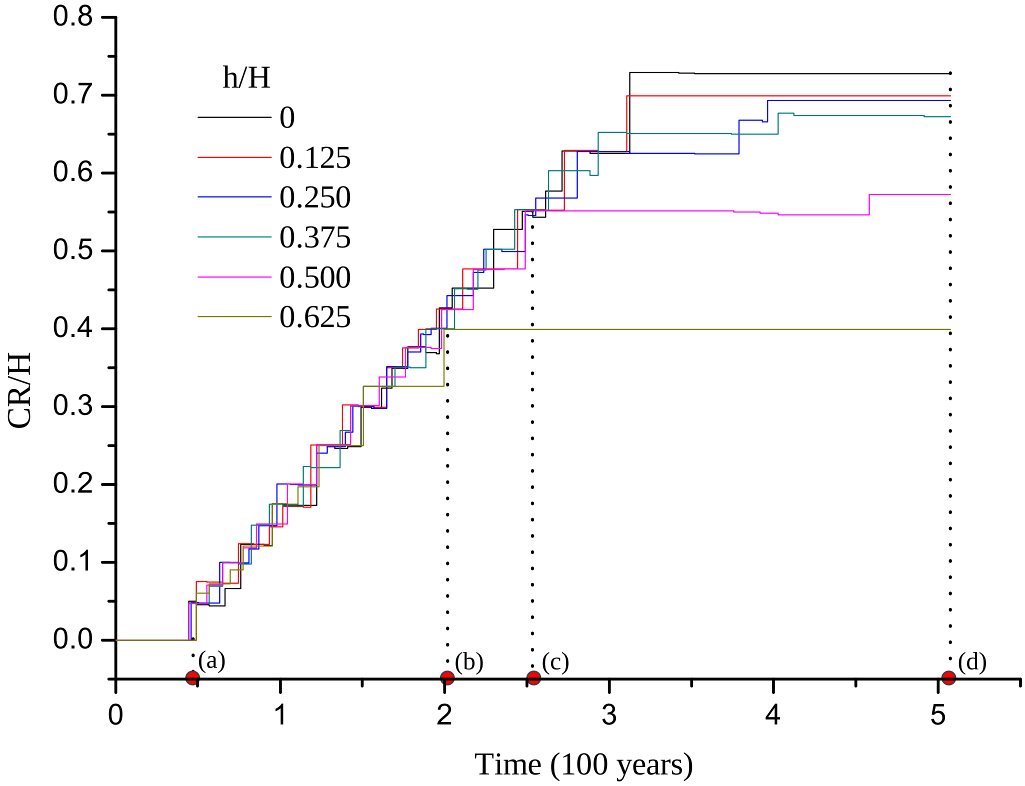

Fig. 17. Dimensionless crest retreat over time.

8. Discussion and conclusions

A novel computational framework called the Nodal-integration based Particle Finite Element Method (N-PFEM) was developed for modelling cliff recession resulting from weathering-caused landslides. To this end, the nodal integration technique is first embedded into the finite element formulation in second-order cone programming. The resulting nodal-integration based finite element formulation (N-FEM) is then merged into the framework of the particle finite element method (PFEM) to form the N-PFEM for simulating cliff recession involving very large material deformations. Comparing to the classical PFEM, the developed N-PFEM stores information of all field variables on mesh nodes and performs nodal integration on the cell associated with each mesh node. Consequently, it requires no operation of variable mapping from old meshes to new meshes, when new meshes are generated, which is essential in the classical PFEM for modelling history-dependent materials and inevitably introduces errors and considerable complexity to solution procedures.

The ability of the proposed N-PFEM for predicting cliff recession in weathering has been showcased through a series of examples. The results from the N-PFEM modelling have been compared with these from the limit analysis, the DEM simulation and the Fisher-Lehmann geomorphologic model available in literatures. Analytical methods, such as the limit analysis method and the Fisher-Lehmann geomorphologic model, can provide a quick estimation of the slope profile. But the limit analysis approach can only handle the weathering-limited case and the shape of the failure surface has to be defined in advance. The simulation results from the N-PFEM and the DEM agree well with each other in terms of both the final deposit shape and the shape of the undisturbed zone of the slope. In comparison with the DEM, the appeal of the N-PFEM is that the time onerous calibration of the material properties at microscopic levels is not required.

The prevention of cliff recession by retaining wall structures is also studied using the developed N-PFEM. Since the purpose of this example is to illustrate the capability of the proposed N-PFEM for studying the effect of a retaining wall on cliff erosions, we only consider a retaining wall of a simple geometry. Further studies on the influences of the geometry and the engineering properties of a retaining wall that may change during the weathering process are critical for the optimum design of retaining walls in practice and achievable using the N-PFEM.

Acknowledgements

We thank the anonymous reviewers and editor for their valuable comments, which have improved the manuscript greatly.

Appendix: Second-order cone programming

In this work, optimisation problem (18) is transformed into a standard SOCP which is then can be resolved using the advanced interior-point method. Very efficient solvers capable of dealing with large-scale SOCP problems have been developed in last decades or so. Of particular notes are the packages MOSEK (Mosek, 2015) and SeDuMi (Sturm, 1999).

The SOCP is a generalization of linear and quadratic programming that allows for affine combinations of variables to be constrained inside a special convex set, called second-order cone (Calafiore and Ghaoui, 2014). The following primal standard form of the SOCP is often used:

$$\begin{array}{ll} \min & \mathbf{a}^{\mathrm{T}}\boldsymbol{y} \\ \text{subject to} & \mathbf{D}\boldsymbol{y} = \boldsymbol{e} \\ & \boldsymbol{y} \in \mathcal{K} \end{array} \tag{A1}$$

where $\boldsymbol{y}$ are the full problem variables and $\mathcal{K}$ is a Cartesian product of second-order cones i.e., $\mathcal{K} = \mathcal{K}_1 \times \mathcal{K}_2 \times \cdots \times \mathcal{K}_n$. Two most common conic cones are:

- the quadratic cone:

$$\mathcal{K}_q = \left\{ \boldsymbol{y} \in \mathbb{R}^m \mid y_1 \geq \sqrt{y_2^2 + \cdots + y_m^2} \right\} \tag{A2}$$

- the rotated quadratic cone:

$$\mathcal{K}_r = \left\{ \boldsymbol{y} \in \mathbb{R}^m \mid 2y_1y_2 \geq y_3^2 + \cdots + y_m^2, y_1 \geq 0,\ y_2 \geq 0 \right\} \tag{A3}$$

The minimisation part of principle (18) with respect to $\Delta\hat{\mathbf{u}}$ can be solved analytically resulting in a maximisation problem:

$$
\begin{aligned}
\max_{\bar{\boldsymbol{\sigma}}_{\mathrm{n+1}},\, \tilde{\boldsymbol{r}}_{\mathrm{n+1}},\, \boldsymbol{p},\, \boldsymbol{q}} \quad & -\frac{1}{2}\Delta\bar{\boldsymbol{\sigma}}_{\mathrm{n+1}}^{\mathrm{T}}\mathbf{C}\Delta\bar{\boldsymbol{\sigma}}_{\mathrm{n+1}} - \frac{1}{2}\Delta t^2 \tilde{\boldsymbol{r}}_{\mathrm{n+1}}^{\mathrm{T}}\mathbf{D}_r\tilde{\boldsymbol{r}}_{\mathrm{n+1}} - \sum_{I=1}^{N_b} g_0^I p^I \\
\text{subject to} \quad & \mathbf{B}^{\mathrm{T}}\bar{\boldsymbol{\sigma}}_{\mathrm{n+1}} + \mathbf{A}^{\mathrm{T}}\tilde{\boldsymbol{r}}_{\mathrm{n+1}} = \tilde{\mathbf{f}} + \boldsymbol{n}\boldsymbol{p} + \hat{\boldsymbol{n}}\boldsymbol{q} \\
& F\left(\bar{\boldsymbol{\sigma}}_{\mathrm{n+1}}\right) \le 0 \\
& F_b\left(\boldsymbol{p},\ \boldsymbol{q}\right) \le 0
\end{aligned}
\tag{A4}
$$

Obviously, this maximum problem is equivalent to the following minimum problem:

$$
\begin{aligned}
\min_{\bar{\boldsymbol{\sigma}}_{\mathrm{n+1}},\, \tilde{\boldsymbol{r}}_{\mathrm{n+1}},\, \boldsymbol{p},\, \boldsymbol{q}} \quad & \frac{1}{2}\Delta\bar{\boldsymbol{\sigma}}_{\mathrm{n+1}}^{\mathrm{T}}\mathbf{C}\Delta\bar{\boldsymbol{\sigma}}_{\mathrm{n+1}} + \frac{1}{2}\Delta t^2 \tilde{\boldsymbol{r}}_{\mathrm{n+1}}^{\mathrm{T}}\mathbf{D}_r\tilde{\boldsymbol{r}}_{\mathrm{n+1}} + \sum_{I=1}^{N_b} g_0^I p^I \\
\text{subject to} \quad & \mathbf{B}^{\mathrm{T}}\bar{\boldsymbol{\sigma}}_{\mathrm{n+1}} + \mathbf{A}^{\mathrm{T}}\tilde{\boldsymbol{r}}_{\mathrm{n+1}} = \tilde{\mathbf{f}} + \boldsymbol{n}\boldsymbol{p} + \hat{\boldsymbol{n}}\boldsymbol{q} \\
& F\left(\bar{\boldsymbol{\sigma}}_{\mathrm{n+1}}\right) \le 0 \\
& F_b\left(\boldsymbol{p},\ \boldsymbol{q}\right) \le 0
\end{aligned}
\tag{A5}
$$

Comparing (A5) to the standard SOCP form (A1), the quadratic terms, namely $\frac{1}{2}\Delta\bar{\boldsymbol{\sigma}}_{\mathrm{n+1}}^{\mathrm{T}}\mathbf{C}\Delta\bar{\boldsymbol{\sigma}}_{\mathrm{n+1}}$ and $\frac{1}{2}\Delta t^2 \tilde{\boldsymbol{r}}_{\mathrm{n+1}}^{\mathrm{T}}\mathbf{D}_r\tilde{\boldsymbol{r}}_{\mathrm{n+1}}$, in the objective function have to be reformulated. To this end, two auxiliary variables X and Y are introduced in the objective function and we have

$$
\begin{aligned}
\min_{\bar{\boldsymbol{\sigma}}_{\mathrm{n+1}},\, \bar{\boldsymbol{r}}_{\mathrm{n+1}},\, \boldsymbol{p},\, \boldsymbol{q}} \quad & X + I + \sum_{I=1}^{N_b} g_0^I p^I \\
\text{subject to} \quad & \mathbf{B}^{\mathrm{T}}\bar{\boldsymbol{\sigma}}_{\mathrm{n+1}} + \mathbf{A}^{\mathrm{T}}\tilde{\boldsymbol{r}}_{\mathrm{n+1}} = \tilde{\mathbf{f}} + \boldsymbol{n}\boldsymbol{p} + \hat{\boldsymbol{n}}\boldsymbol{q} \\
& X \ge \frac{1}{2}\Delta\bar{\boldsymbol{\sigma}}_{\mathrm{n+1}}^{\mathrm{T}}\mathbf{C}\Delta\bar{\boldsymbol{\sigma}}_{\mathrm{n+1}} \\
& I \ge \frac{1}{2}\Delta t^2 \tilde{\boldsymbol{r}}_{\mathrm{n+1}}^{\mathrm{T}}\mathbf{D}_r\tilde{\boldsymbol{r}}_{\mathrm{n+1}} \\
& F\left(\bar{\boldsymbol{\sigma}}_{\mathrm{n+1}}\right) \le 0 \\
& F_b\left(\boldsymbol{p},\ \boldsymbol{q}\right) \le 0
\end{aligned}
\tag{A6}
$$

The newly introduced inequality constraints can be converted to rotated quadratic cones:

$$
\begin{aligned}
&\min_{\bar{\boldsymbol{\sigma}}_{\mathrm{n}+1},\, \bar{\boldsymbol{r}}_{\mathrm{n}+1},\, \boldsymbol{p},\, \boldsymbol{q}} \quad X + I + \sum_{I=1}^{N_b} g_0^I p^I \\
&\text{subject to } \ \mathbf{B}^{\mathrm{T}} \bar{\boldsymbol{\sigma}}_{\mathrm{n}+1} + \mathbf{A}^{\mathrm{T}} \tilde{\boldsymbol{r}}_{\mathrm{n}+1} = \tilde{\mathbf{f}} + \boldsymbol{n}\boldsymbol{p} + \hat{\boldsymbol{n}}\boldsymbol{q} \\
&\qquad\qquad \boldsymbol{\xi}_{\bar{\boldsymbol{\sigma}}} = \mathbf{C}^{-\frac{1}{2}} \Delta \bar{\boldsymbol{\sigma}}_{\mathrm{n}+1},\ Y = 1,\ (X, Y, \boldsymbol{\xi}_{\bar{\boldsymbol{\sigma}}}) \in \mathcal{K}_r \\
&\qquad\qquad \mathcal{K}_r = \left\{ (X, Y, \boldsymbol{\xi}_{\bar{\boldsymbol{\sigma}}}) \in \mathbb{R}^{m+2} \mid 2XY \geq \boldsymbol{\xi}_{\bar{\boldsymbol{\sigma}}}^{\mathrm{T}} \boldsymbol{\xi}_{\bar{\boldsymbol{\sigma}}},\ X \geq 0,\ Y \geq 0 \right\} \\
&\qquad\qquad \boldsymbol{\xi}_{\bar{\boldsymbol{r}}} = \Delta t \mathbf{D}_r^{-\frac{1}{2}} \tilde{\boldsymbol{r}}_{\mathrm{n}+1},\ J = 1,\ (I, J, \boldsymbol{\xi}_{\bar{\boldsymbol{r}}}) \in \mathcal{K}_r \\
&\qquad\qquad \mathcal{K}_r = \left\{ (I, J, \boldsymbol{\xi}_{\bar{\boldsymbol{r}}}) \in \mathbb{R}^{m+2} \mid 2IJ \geq \boldsymbol{\xi}_{\bar{\boldsymbol{r}}}^{\mathrm{T}} \boldsymbol{\xi}_{\bar{\boldsymbol{r}}},\ X \geq 0,\ Y \geq 0 \right\} \\
&\qquad\qquad F\left(\bar{\boldsymbol{\sigma}}_{\mathrm{n}+1}\right) \leq 0 \\
&\qquad\qquad F_b\left(\boldsymbol{p},\ \boldsymbol{q}\right) \leq 0
\end{aligned}
\tag{A7}
$$

The yield criteria $F\left(\bar{\boldsymbol{\sigma}}_{\mathrm{n}+1}\right) \leq 0$ and $F_b\left(\boldsymbol{p},\ \boldsymbol{q}\right) \leq 0$ can be reformulated as a quadratic cone as well. Readers are referred to (Zhang et al., 2013) for more details. Problem (A7) is now the formulation of the N-FEM in a standard SOCP form which is the eventual problem to be resolved at each incremental analysis step.

References

Andersen, S. and Andersen, L. 2010. "Modelling of landslides with the material-point method." *Computational Geosciences* 14(1): 137-147.

Andrews, D. and Bucknam, R. C. 1987. "Fitting degradation of shoreline scarps by a nonlinear diffusion model." *Journal of Geophysical Research: Solid Earth* 92(B12): 12857-12867.

Bakker, J. P. and Le Heux, J. 1946. Projective-geometric treatment of O. Lehmann's theory of the transformation of steep mountain slopes, *north. Holland publ.*

Bird, E. 2016. Rates of Cliff Recession. *Coastal Cliffs: Morphology and Management*. Cham, Springer International Publishing**:** 59-64.

Bray, M. J. and Hooke, J. M. 1997. "Prediction of Soft-Cliff Retreat with Accelerating Sea-Level Rise." *Journal of Coastal Research* 13(2): 453-467.

Bui, H. H., Fukagawa, R., Sako, K. and Wells, J. C. 2011. "Slope stability analysis and discontinuous slope failure simulation by elasto-plastic smoothed particle hydrodynamics (SPH)." *Géotechnique* 61(7): 565-574.

Calafiore, G. C. and Ghaoui, L. E. 2014. Optimization models, *Cambridge University Press*.

Cante, J., Dávalos, C., Hernández, J. A., Oliver, J., Jonsén, P., Gustafsson, G. and Häggblad, H. Å. 2014. "PFEM-based modeling of industrial granular flows." *Computational Particle Mechanics* 1(1): 47-70.

Carbonell, J. M., Oñate, E. and Suárez, B. 2010. "Modeling of Ground Excavation with the Particle Finite-Element Method." *Journal of Engineering Mechanics* 136(4): 455-463.

Favreau, P., Mangeney, A., Lucas, A., Crosta, G. and Bouchut, F. 2010. "Numerical modeling of landquakes." *Geophysical Research Letters* 37(15).

Fisher, O. 1866. "On the Disintegration of a Chalk Cliff." *Geological Magazine* 3(26): 354-356.

Franci, A. and Cremonesi, M. 2019. "3D regularized μ(I)-rheology for granular flows simulation." *Journal of Computational Physics* 378: 257-277.

Franci, A., Cremonesi, M., Perego, U. and Oñate, E. 2020. "A Lagrangian nodal integration method for free-surface fluid flows." *Computer Methods in Applied Mechanics and Engineering* 361: 112816.

Gullà, G., Mandaglio, M. C. and Moraci, N. 2006. "Effect of weathering on the compressibility and shear strength of a natural clay." *Canadian Geotechnical Journal* 43(6): 618-625.

Gupta, A. and Rao, K. S. 2000. "Weathering effects on the strength and deformational behaviour of crystalline rocks under uniaxial compression state." *Engineering Geology* 56(3-4): 257-274.

Hobbs, P. R. N., Jones, L. D., Kirkham, M. P., Pennington, C. V. L., Morgan, D. J. R. and Dashwood, C. 2020. "Coastal landslide monitoring at Aldbrough, East Riding of Yorkshire, UK." *Quarterly Journal of Engineering Geology and Hydrogeology* 53(1): 101-116.

Hutchinson, J. 1998. "A small ‐ scale field check on the Fisher–Lehmann and Bakker–Le Heux cliff degradation models." *Earth Surface Processes and Landforms: The Journal of the British Geomorphological Group* 23(10): 913-926.

Hutchinson, J. N. 2001. "The Fourth Glossop Lecture: Reading the Ground: Morphology and Geology in Site Appraisal." *Quarterly Journal of Engineering Geology and Hydrogeology* 34(1): 7-50.

Idelsohn, S. R., Oñate, E. and Pin, F. D. 2004. "The particle finite element method: a powerful tool to solve incompressible flows with free ‐ surfaces and breaking waves." *International journal for numerical methods in engineering* 61(7): 964-989.

Kimmance, J. P. 1988. Computer aided risk analysis of open pit mine slopes in Kaolin mineral deposits. Degree of Doctor of Philosophy, Royal School of Mines - Imperial College.

Kogure, T., Aoki, H., Maekado, A., Hirose, T. and Matsukura, Y. 2006. "Effect of the development of notches and tension cracks on instability of limestone coastal cliffs in the Ryukyus, Japan." *Geomorphology* 80(3-4): 236-244.

Krabbenhoft, K., Lyamin, A., Huang, J. and da Silva, M. V. 2012. "Granular contact dynamics using mathematical programming methods." *Computers and Geotechnics* 43: 165-176.

Krabbenhøft, K., Lyamin, A. and Sloan, S. 2007. "Formulation and solution of some plasticity problems as conic programs." *International Journal of Solids and Structures* 44(5): 1533-1549.

Lagrée, P.-Y., Staron, L. and Popinet, S. 2011. "The granular column collapse as a continuum: validity of a two-dimensional Navier-Stokes model with a [mu](I)-rheology." *Journal of Fluid Mechanics* 686: 378.

Lehmann, O. 1933. "Morphologische theorie der verwitterung von steinschlagwanden." *Vierteljahrsschrift der Naturforschenden Gesellschaft in Zurich* 78(21): 83-126.

Liu, G.-R. and Trung, N. 2010. Smoothed finite element methods. 6000 Broken Sound Parkway NW, Suite 300, *CRC press*.

Liu, G., Nguyen-Thoi, T., Nguyen-Xuan, H. and Lam, K. 2009. "A node-based smoothed finite element method (NS-FEM) for upper bound solutions to solid mechanics problems." *Computers & structures* 87(1-2): 14-26.

Lucas, A. and Mangeney, A. 2007. "Mobility and topographic effects for large Valles Marineris landslides on Mars." *Geophysical research letters* 34(10).

Mangeney ‐ Castelnau, A., Vilotte, J. P., Bristeau, M.-O., Perthame, B., Bouchut, F., Simeoni, C. and Yerneni, S. 2003. "Numerical modeling of avalanches based on Saint Venant equations using a kinetic scheme." *Journal of Geophysical Research: Solid Earth* 108(B11).

Mangeney, A., Bouchut, F., Thomas, N., Vilotte, J.-P. and Bristeau, M. 2007a. "Numerical modeling of self ‐ channeling granular flows and of their levee ‐ channel deposits." *Journal of Geophysical Research: Earth Surface* 112(F2).

Mangeney, A., Tsimring, L., Volfson, D., Aranson, I. S. and Bouchut, F. 2007b. "Avalanche mobility induced by the presence of an erodible bed and associated entrainment." *Geophysical Research Letters* 34(22).

Massey, C., Della Pasqua, F., Holden, C., Kaiser, A., Richards, L., Wartman, J., McSaveney, M., Archibald, G., Yetton, M. and Janku, L. 2017. "Rock slope response to strong earthquake shaking." *Landslides* 14(1): 249-268.

Meng, J., Cao, P., Huang, J., Lin, H., Chen, Y. and Cao, R. 2019a. "Second-order cone programming formulation of discontinuous deformation analysis." *International Journal for Numerical Methods in Engineering* 118(5): 243-257.

Meng, J., Huang, J., Lin, H., Laue, J. and Li, K. 2019b. "A static discrete element method with discontinuous deformation analysis." *International Journal for Numerical Methods in Engineering* 120(7): 918-935.

Meng, J., Huang, J., Yao, C. and Sheng, D. 2018. "A discrete numerical method for brittle rocks using mathematical programming." *Acta Geotechnica* 13: 283-302.

Monforte, L., Arroyo, M., Carbonell, J. M. and Gens, A. 2017. "Numerical simulation of undrained insertion problems in geotechnical engineering with the Particle Finite Element Method (PFEM)." *Computers and Geotechnics* 82: 144-156.

Mosek, A. 2015. The MOSEK optimization toolbox for MATLAB manual. *Version 7.1 (Revision 28)*.

Mulligan, R. P., Franci, A., Celigueta, M. A. and Take, W. A. 2020. "Simulations of Landslide Wave Generation and Propagation Using the Particle Finite Element Method." *Journal of Geophysical Research: Oceans* 125(6): e2019JC015873.

Nash, D. B. 1981. "FAULT: A FORTRAN program for modeling the degradation of active normal fault scarps." *Computers & Geosciences* 7(3): 249-266.

Oñate, E., Celigueta, M. A., Idelsohn, S. R., Salazar, F. and Suárez, B. 2011. "Possibilities of the particle finite element method for fluid–soil–structure interaction problems." *Computational Mechanics* 48(3): 307.

Oñate, E., Idelsohn, S. R., Del Pin, F. and Aubry, R. 2004. "The Particle Finite Element Method - An Overview." *International Journal of Computational Methods* 01(02): 267-307.

Pastor, M., Blanc, T., Haddad, B., Petrone, S., Sanchez Morles, M., Drempetic, V., Issler, D., Crosta, G. B., Cascini, L., Sorbino, G. and Cuomo, S. 2014. "Application of a SPH depth-integrated model to landslide run-out analysis." *Landslides* 11(5): 793-812.

Soga, K., Alonso, E., Yerro, A., Kumar, K. and Bandara, S. 2016. "Trends in large-deformation analysis of landslide mass movements with particular emphasis on the material point method." *Géotechnique* 66(3): 248-273.

Staron, L. 2008. "Mobility of long-runout rock flows: a discrete numerical investigation." *Geophysical Journal International* 172(1): 455-463.

Staron, L. and Hinch, E. 2005. "Study of the collapse of granular columns using DEM numerical simulation." *Journal of Fluid Mechanics* 545: 1-27.

Staron, L., Lagrée, P.-Y. and Popinet, S. 2014. "Continuum simulation of the discharge of the granular silo." *The European Physical Journal E* 37(1): 5.

Sturm, J. F. 1999. "Using SeDuMi 1.02, a MATLAB toolbox for optimization over symmetric cones." *Optimization methods and software* 11(1-4): 625-653.

Sunamura, T. 1982. "A predictive model for wave-induced cliff erosion, with application to Pacific coasts of Japan." *The Journal of Geology* 90(2): 167-178.

Tran, Q.-A. and Sołowski, W. 2019. "Generalized Interpolation Material Point Method modelling of large deformation problems including strain-rate effects – Application to penetration and progressive failure problems." *Computers and Geotechnics* 106: 249-265.

Tran, T. V., Alkema, D. and Hack, R. 2019. "Weathering and deterioration of geotechnical properties in time of groundmasses in a tropical climate." *Engineering geology* 260: 105221.

Utili, S. and Crosta, G. B. 2011a. "Modeling the evolution of natural cliffs subject to weathering: 1. Limit analysis approach." *Journal of Geophysical Research: Earth Surface* 116(F1).

Utili, S. and Crosta, G. B. 2011b. "Modeling the evolution of natural cliffs subject to weathering: 2. Discrete element approach." *Journal of Geophysical Research: Earth Surface* 116(F1).

Utili, S. and Nova, R. 2008. "DEM analysis of bonded granular geomaterials." *International Journal for Numerical and Analytical Methods in Geomechanics* 32(17): 1997-2031.

Voulgari, C. and Utili, S. 2017. "A general analytical solution for the evolution of cliffs accounting for strength degradation, seismic action, formation of tension cracks and seepage." *Engineering Geology* 219: 92-106.

Wang, L., Zhang, X., Zaniboni, F., Oñate, E. and Tinti, S. 2019. "Mathematical Optimization Problems for Particle Finite Element Analysis Applied to 2D Landslide Modeling." *Mathematical Geosciences*: DOI: 10.1007/s11004-11019-09837-11001 (in press).

Wang, Y. and Leung, S. 2008. "Characterization of cemented sand by experimental and numerical investigations." *Journal of geotechnical and geoenvironmental engineering* 134(7): 992-1004.

Xue, Z., Feng, A., Yin, P. and Xia, D. 2009. "Coastal erosion induced by human activities: A northwest Bohai Sea case study." *Journal of Coastal Research* 25(3 (253)): 723-733.

Yokota, S. and Iwamatsu, A. 2000. Weathering distribution in a steep slope of soft pyroclastic rocks as an indicator of slope instability. *Developments in geotechnical engineering*, Elsevier. 84**:** 187-198.

Yuan, W.-H., Liu, K., Zhang, W., Dai, B. and Wang, Y. 2020. "Dynamic modeling of large deformation slope failure using smoothed particle finite element method." *Landslides* 17(7): 1591-1603.

Yuan, W.-H., Wang, B., Zhang, W., Jiang, Q. and Feng, X.-T. 2019. "Development of an explicit smoothed particle finite element method for geotechnical applications." *Computers and Geotechnics* 106: 42-51.

Zhang, K., Tan, P., Ma, G. and Cao, P. 2016. "Modeling of the progressive failure of an overhang slope subject to differential weathering in Three Gorges Reservoir, China." *Landslides* 13(5): 1303-1313.

Zhang, W., Yuan, W. and Dai, B. 2018. "Smoothed particle finite-element method for large-deformation problems in geomechanics." *International Journal of Geomechanics* 18(4): 04018010.

Zhang, X., Krabbenhoft, K., Pedroso, D., Lyamin, A., Sheng, D., Da Silva, M. V. and Wang, D. 2013. "Particle finite element analysis of large deformation and granular flow problems." *Computers and Geotechnics* 54: 133-142.

Zhang, X., Krabbenhoft, K., Sheng, D. and Li, W. 2014. "Numerical simulation of a flow-like landslide using the particle finite element method." *Computational Mechanics* 55(1): 167-177.

Zhang, X., Oñate, E., Torres, S. A. G., Bleyer, J. and Krabbenhoft, K. 2019a. "A unified Lagrangian formulation for solid and fluid dynamics and its possibility for modelling submarine landslides and their consequences." *Computer Methods in Applied Mechanics and Engineering* 343: 314-338.

Zhang, X., Sheng, D., Sloan, S. W. and Bleyer, J. 2017. "Lagrangian modelling of large deformation induced by progressive failure of sensitive clays with elastoviscoplasticity." *International Journal for Numerical Methods in Engineering* 112(8): 963-989.

Zhang, X., Wang, L., Krabbenhoft, K. and Tinti, S. 2019b. "A case study and implication: particle finite element modelling of the 2010 Saint-Jude sensitive clay landslide." *Landslides* 17(5): 1117-1127.